ANL/NSE-21/54

Evaluation of China Experimental Fast Reactor Start-up Tests – Final Report

Nuclear Science and Engineering Division

About Argonne National Laboratory

Argonne is a U.S. Department of Energy laboratory managed by UChicago Argonne, LLC under contract DE-AC02-06CH11357. The Laboratory's main facility is outside Chicago, at 9700 South Cass Avenue, Argonne, Illinois 60439. For information about Argonne and its pioneering science and technology programs, see www.anl.gov.

DOCUMENT AVAILABILITY

Online Access: U.S. Department of Energy (DOE) reports produced after 1991 and a growing number of pre-1991 documents are available free at OSTI.GOV (http://www.osti.gov/), a service of the US Dept. of Energy's Office of Scientific and Technical Information.

Reports not in digital format may be purchased by the public from the National Technical Information Service (NTIS):

U.S. Department of Commerce
National Technical Information Service
5301 Shawnee Rd
Alexandria, VA 22312
www.ntis.gov
Phone: (800) 553-NTIS (6847) or (703) 605-6000
Fax: (703) 605-6900
Email: **orders@ntis.gov**

Reports not in digital format are available to DOE and DOE contractors from the Office of Scientific and Technical Information (OSTI):

U.S. Department of Energy
Office of Scientific and Technical Information
P.O. Box 62
Oak Ridge, TN 37831-0062
www.osti.gov
Phone: (865) 576-8401
Fax: (865) 576-5728
Email: **reports@osti.gov**

Disclaimer

This report was prepared as an account of work sponsored by an agency of the United States Government. Neither the United States Government nor any agency thereof, nor UChicago Argonne, LLC, nor any of their employees or officers, makes any warranty, express or implied, or assumes any legal liability or responsibility for the accuracy, completeness, or usefulness of any information, apparatus, product, or process disclosed, or represents that its use would not infringe privately owned rights. Reference herein to any specific commercial product, process, or service by trade name, trademark, manufacturer, or otherwise, does not necessarily constitute or imply its endorsement, recommendation, or favoring by the United States Government or any agency thereof. The views and opinions of document authors expressed herein do not necessarily state or reflect those of the United States Government or any agency thereof, Argonne National Laboratory, or UChicago Argonne, LLC.

ANL/NSE-21/54

Evaluation of China Experimental Fast Reactor Start-up Tests - Final Report

prepared by

Taek K. Kim, Michael Jarrett, Zhaopeng Zhong, and Changho Lee

Nuclear Science and Engineering Division
Argonne National Laboratory

September 30, 2021

EXECUTIVE SUMMARY

This report documents the results and observations on the Coordinated Research Project (CRP) of the International Atomic Energy Agency (IAEA) on "*Neutronics Benchmark of CEFR Start-Up Tests.*" The China Experimental Fast Reactor (CEFR) is a 65MWt sodium-cooled fast reactor with highly enriched uranium oxide fuels. The reactor achieved the first criticality in 2010, and series of start-up tests were conducted to measure various reactor physics parameters. In 2018, IAEA has launched the CRP for validation and qualification of member states' computation capabilities in the field of fast reactor simulation utilizing the measured data in the CEFR start-up test. Twenty-nine international organizations from eighteen member countries, including Argonne National Laboratory, have participated in the CRP.

The neutronics benchmark consists of six experimental measurements, criticality per fuel loading, control rod worth, sodium void reactivity, temperature reactivity, subassembly swap reactivity, and foil activation measurements. Participants also agreed on a numerical benchmark for the evaluation of integral reactivity coefficients related to the safety feature of the CEFR core. The Chinese Institute of Atomic Energy (CIAE) provided the benchmark specifications, drawings, measured data, and experimental uncertainties.

The CRP has been conducted based on two phases. The first phase was a blind benchmark without measured data, and the second phase was an open benchmark with measured data. In the open benchmark, all participants could access the measured data and the results from other participants. Both phases have been completed, and participants are writing the IAEA technology document, which will be published in 2022.

In this work, the CEFR start-up test parameters were simulated using the Argonne Reactor Computation (ARC) code suite, i.e., MC^2-3/TWODANT, DIF3D-VARIANT, and PERSENT. The input preparation was performed using the PyARC script to generate input files for each case.

The whole core was simulated using the region and material dependent 33-group cross sections. The results are generally well agreed with the measurements. For instance, the calculated core multiplication factor for the given CEFR critical configuration is 0.99890, which is 110 pm lower than the criticality. Other parameters, such as control rod worth, sodium void worth, temperature reactivity coefficient, subassembly swap reactivity, and foil activation rates, are aggreged with the measured values within the one standard deviation of the experimental uncertainties. A noticeable discrepancy between calculation and measurement was observed in the Au-197 (n,γ) reaction rates in the radial reflector and axial blankets. The primary reason for the discrepancy was poor modeling of the spatial self-shielding effect of the Au-197 (n,γ) reaction in the epithermal energy range. In this work, the discrepancy was resolved by modeling the spatial self-shielding effect in the MC^2-3 calculations and refining the cross-section group structures.

The CRP was a good opportunity to validate ARC code suite by comparing the results with the measured data and the results calculated by various participants with both deterministic and stochastic reactor analysis codes. Additionally, the followings are observed in the CRP:

- Except for several outliers, the accuracies of both deterministic calculations and stochastic calculations are comparable to each other (see the comparison of criticality

and sodium void worth in Figure 4.2 and Figure 4.6, respectively). Note that the outliers are mainly due to the misunderstanding of the experiments or inaccurate cross sections.

- The results could be different even though the same reactor analysis codes were used. For instance, several participants used the DIF3D and Serpent codes for deterministic and stochastic calculations, respectively. However, as shown in Figure 4.2, the results are different depending on the neutron libraries, cross sections generation methods, and modeling of the core. This observation informs that experiences of fast reactor analyses and knowledge on computation codes are important factors to have accurate results.
- Reactor-specific physics and material characteristics should be well captured in the modeling and simulation. Otherwise, calculated reactor physics parameters may contain large errors as observed in the Au-197 (n,γ) activation measurement (see section 4.6 and section 6).

TABLE OF CONTENTS

Executive summary 1
Table of Contents 3
List of Figures 5
List of Tables 7
1. Introduction 9
2. CEFR Technical Specifications 10
3. CEFR Model and Calculation Methodologies 16
3.1 Fuel subassembly Model 16
3.2 Control subassembly Model 18
3.3 Reflector subassembly Model 18
3.4 Shield subassembly Model 18
3.5 Mock Fuel subassembly Models 19
3.6 Summary of Changes 19
4. Benchmark Comparison to Experimental Measurements 20
4.1 Approach to criticality per loading of fuel subassemblies 20
4.2 Control rod worth measurements 22
4.3 Sodium void reactivity worth 27
4.4 Temperature reactivity coefficient 29
4.5 Subassembly swap reactivity 31
4.6 Foil reaction rate measurements 34
5. Reactor Safety Parameters 41
5.1 Kinetics Parameters 41
5.2 Doppler coefficient and sodium void worth 41
5.3 Axial and radial expansion coefficients 43
5.4 Control rod expansion coefficients 45
5.5 Density reactivity coefficients 46
6. Further Investigation on Au-197 Foil Activation 49
6.1 Investigation topics and computation models 49
6.2 Comparison of revised Au-197 (n,γ) reaction rate 50

7. Conclusions and Observations.....54
References.....56
Appendix A. List of Paticipants 57
Appendix B. Foil Isotope Cross Sections 58
Appendix C. investigation on cross-section group structure 62

LIST OF FIGURES

Figure 2.1 CEFR reactor axial configuration 11
Figure 2.2 CEFR Core radial configuration 12
Figure 2.3 Locations of start-up detectors and source-range detectors 15
Figure 3.1 TWODANT 2D R-Z geometry for ultra-fine group spectrum calculation 17
Figure 4.1. Core configuration for approach to criticality 20
Figure 4.2 Prediction of criticality by participants 22
Figure 4.3. CEFR basic core layout for control worth measurement 23
Figure 4.4 Integral worth for each control subassembly 26
Figure 4.5 subassembly locations for sodium void measurements 28
Figure 4.6 Comparison of sodium void worth 29
Figure 4.7 Comparison of temperature reactivity coefficient 31
Figure 4.8 Locations for subassembly swap reactivity measurement 32
Figure 4.9 Comparison of swap reactivities 33
Figure 4.10 Radial locations for foil activation measurements 34
Figure 4.11 Radial distribution of measured foil activation 36
Figure 4.12 Axial distribution of measured foil activation 37
Figure 4.13 Comparison of radial U-235 (n,f) reaction rate distribution 38
Figure 4.14 Comparison of axial U-235 (n,f) reaction rate distribution 39
Figure 4.15 Comparison of radial Au-197 (n,γ) reaction rate distribution 39
Figure 4.16 Comparison of axial Au-197 (n,γ) reaction rate distribution 40
Figure 5.1 Comparison of Doppler constant at normal operation condition 42
Figure 5.2 Comparison of Doppler constant at sodium voided condition 43
Figure 5.3 Comparison of axial expansion coefficients 44
Figure 5.4 Comparison of radial expansion coefficients 45
Figure 5.5 Comparison of regulating control rod expansion coefficients 45
Figure 5.6 Comparison of shim control rod expansion coefficients 46
Figure 5.7 Comparison of fuel density coefficients 47
Figure 5.8 Comparison of steel density coefficients 48
Figure 5.9 Comparison of sodium density coefficients 48

Figure 6.1 Comparison of the continuous energy and 68-group Au^{197} (n,γ) cross sections 50
Figure 6.2 One-dimensional heterogeneous models of MC^2-3 for experimental SAs.....50
Figure 6.4 Axial profiles of Au^{197}(n,γ) reaction rate 52
Figure 6.6 Radial profiles of Au^{197}(n,γ) reaction rate 52

Figure B.1 Al-27 (n,α) ENDF/B-VIII.0 cross section data 58
Figure B.2 Ni-58 (n,p) cross section ENDF/B-VIII.0 cross section data 59
Figure B.3 Au-197 (n,γ) ENDF/B-VIII.0 cross section data 59
Figure B.4 U-235 (n,f) ENDF/B-VIII.0 cross section data 60
Figure B.5 U-238 (n,f) ENDF/B-VIII.0 cross section data 60
Figure B.6 Np-237 (n,f) ENDF/B-VIII.0 cross section data 61

Figure C.1 Flux, cross section, and Au-197 (n,γ) reaction rate in radial reflector.....63
Figure C.2 70 group flux, cross section, and reaction rate for Au-197 neutron capture 65

LIST OF TABLES

Table 2.1 Main parameters of CEFR Core 13
Table 2.2 Main Parameters of Subassemblies 13
Table 2.3 Expansion Coefficients 14
Table 2.4 Information of fuel rod 14
Table 2.5 Total mass of fuel/blanket in each fuel SA 14
Table 2.6 Total mass of absorber in each control SA 14
Table 2.7 Neutron Detectors in CEFR 15
Table 3.1 Steel composition (mass fraction) for fuel and structural steels 17
Table 4.1 Approach to criticality at 250°C 21
Table 4.2 Control rod worth measurement 24
Table 4.3 Comparison of calculated control rod worth with measurement 25
Table 4.4 Control rod worth of individual subassembly and banks for full insertion 25
Table 4.5 Integral worth for each rod at 50 mm intervals 26
Table 4.6 Differential worth for each rod at 50 mm intervals 26
Table 4.7 Voided subassembly experiment, no control rod movement 28
Table 4.8 Measurement data of temperature reactivity coefficient 30
Table 4.9 Temperature reactivity coefficient 30
Table 4.10 Subassembly swap reactivity 33
Table 4.11 Radial foil activation measurement 34
Table 4.12 Axial foul activation measurement 35
Table 4.13 Radial distribution of calculated activation foil reaction rates 37
Table 4.14 Axial distribution of calculated activation foil reaction rates 38
Table 5.1 Kinetics parameters for Operating Cold State (250˚C) 41
Table 5.2 Doppler coefficient at normal and voided conditions 42
Table 6.2 Axial reaction rate distribution of Au197(n,γ) reaction rate 51
Table 6.4 Radial reaction rate distribution of Au197(n,γ) reaction rate 51

Table A. 1 List of participants using deterministic codes 57

Table C.1 Relative Au-197 (n,γ) reaction rate contribution per different energy regimes 62
Table C.2 Radial distribution of Au-197 neutron capture reaction rate 64
Table C.3 Axial distribution of Au-197 neutron capture reaction rate 64

1. Introduction

The China Experimental Fast Reactor (CEFR) is a 65 MW-thermal pool-type Sodium-cooled Fast Reactor (SFR), located at the China Institute of Atomic Energy (CIAE) in Beijing. The first criticality was achieved in 2010, and a series of start-up tests was followed to measure various reactor physics parameters. The start-up tests include the measurements of the neutron multiplication factor change depending on the fuel loadings, control rod worth, sodium-void worth, temperature reactivity coefficients, foil activations, etc. In 2018, the International Atomic Energy Agency (IAEA) has launched a Coordinated Research Project (CRP) of on "*Neutronics Benchmark of CEFR Start-Up Test,"* for validation and qualification of member states computation capabilities in the field of fast reactor simulation utilizing the CEFR start-up test (IAEA 2018). Twenty-nine international organizations from eighteen member countries, including Argonne National Laboratory, have participated in the CRP. The participants are listed in Appendix A, including the computation codes.

The Chinese Institute of Atomic Energy (CIAE) provided the benchmark specifications in the kick-off meeting in 2018, and the benchmark specifications were iteratively revised to accommodate the comments and suggestions of participants. In particular, the benchmark specifications were finalized using the measured compositions data rather than the nominal design values. In addition, the complicate upper and lower structures of fuel subassemblies were simplified, and the measurement uncertainties are included.

The CRP consists of two phases for three years. The first phase is a blind benchmark, and the second phase is an open benchmark. In the blind benchmark, each participant simulated the start-up tests using the given benchmark specifications without the measured data. In the open benchmark, however, all participants could access the measured data and the results from other participants. The blind phase was completed in 2019, and results from the open benchmark were shared with the participants in April 2021. The blind benchmark results are reported by Jarrett et al. (2019), and this report summarizes the open benchmark results.

Argonne National Laboratory has participated in the CRP using the Argonne Reactor Computation (ARC) fast reactor code suite. The ARC code suite has been developed and validated through various fast reactor programs. The CRP provides additional opportunity to validate the ARC code suite based on the measured data through the CEFR start-up test and those from international participants using various computation codes. This will help to define the role of ARC code suite in the current landscape of fast reactor development and clearly define any potential limitations.

After short summary of the CEFR benchmark specifications in Section 0, the model developed with the ARC codes is briefly described in Section 3; more detail is given in the blind phase report from the previous year (Jarrett 2019). The main benchmark results are described in Sections 0, 0, and 6, with comparisons to the results from other participants. Finally, the conclusions of this analysis are discussed in Section 7.

2. CEFR Technical Specifications

CIAE provided the CEFR core technical specifications and the start-up tests information, which have been revised several times. The technical specifications for the blind benchmark were released in 2018 (Huo 2018). During the blind benchmark phase, participants requested a detailed information on the fuel compositions and drawings of fuel and experiment subassemblies. The technical specification has been revised to accommodate the information requests by participants, and the latest version (version 7) was released in December 2019 for the open benchmark (Huo 2019). In particular, the fuel compositions and dimensions are provided as the measured values with uncertainties in the latest version of the technical specifications, which were provided as nominal design values without uncertainties in the previous versions of the technical specifications.

The CEFR reactor and core configurations are plotted in Figure 2.1 and Figure 2.2, respectively, and the main core parameters are given in

Table 2.1, and the detailed sub-assembly information is given in Table 2.2 at the installation temperature of 20 ^{o}C.

The inner diameter of the main vessel is about 8 m. The subassembly pitch is 6.1 cm with 61 fuel pins. The height of the driver fuel is 45 cm; thus, the driver region aspect ratio is 0.75. There is also a 25 cm lower axial blanket and 10 cm upper axial blanket.

The driver fuel employs highly enriched uranium (HEU) oxide (64.4wt% U-235) with a central hole that is approximately 1.6 mm in diameter. There are eight B_4C control assemblies. There are three safety assemblies, three shim assemblies, and two regulating assemblies. The safety and shim rods use 92 at% B-10, and the regulating rods use natural boron. The shim rods are for large adjustments to core reactivity, the regulating rods are for fine adjustment, and the safety rods are a backup shutdown system.

The material specifications are “as manufactured” with an assumed temperature of 20°C. The “cold” operating temperature of the core is 250°C, so the dimensions and densities of the materials must be adjusted to account for thermal expansion. The thermal expansion coefficients are given in

Table 2.3.

The design value of fuel rods and measured masses of fuel and blanket subassemblies are provided in Table 2.4 and Table 2.5, respectively. In the open benchmark, it was recommended to use the mass values in Table 2.5, rather than design densities in Table 2.4. The B_4C in shim rods and safety rods contains enriched B-10, while the B-10 in regulating rods is at natural abundance. The total mass of B_4C is given in Table 2.6, which are measured values.

Table 2.7 shows the detectors installed in the CEFR and the locations of start-up and source-range detectors are shown in Figure 2.3. For safety feature, at least two neutron detection systems are working during normal operation.

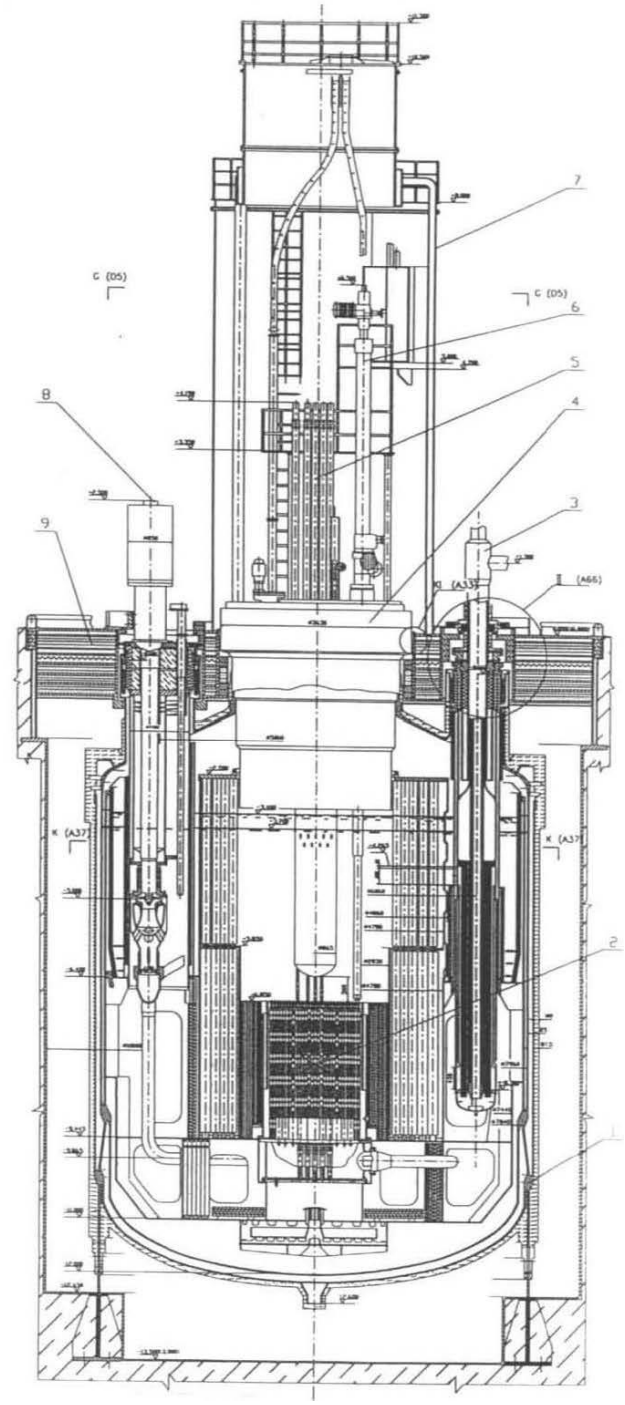

1. Main Vessel
2. Reactor Core
3. Intermediate heat exchanger
4. Rotating plug
5. Control Rod Driving Mechanism
6. Fuelling Machine
7. Protective Cover
8. Main Pump
9. Fixed Shielding

Figure 2.1 CEFR reactor axial configuration

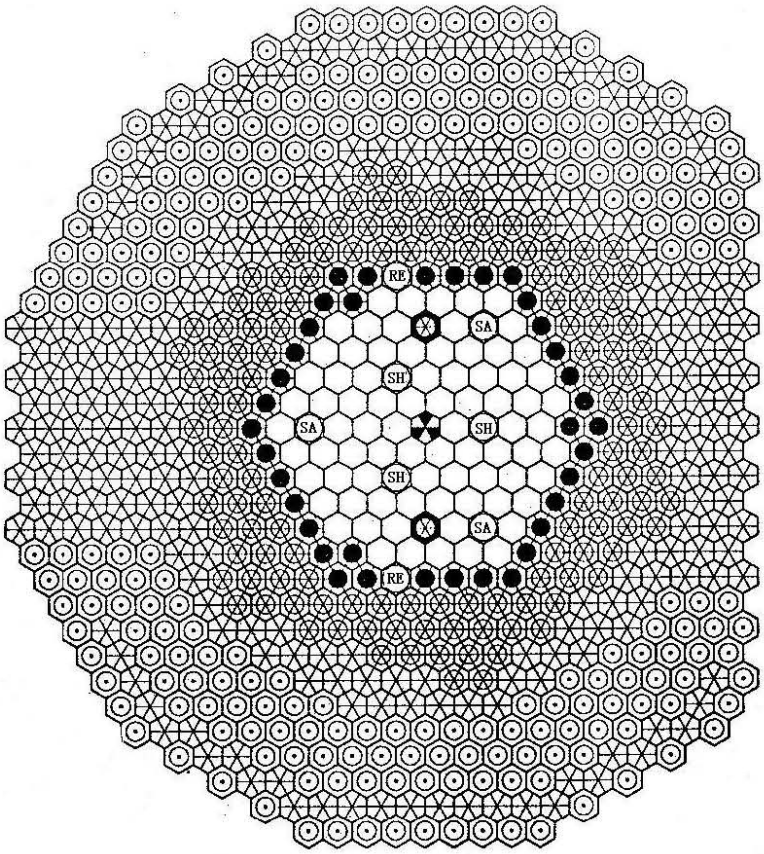

Legend	Assembly Type	Number
	Fuel Assembly	79
	1-Steel Shielding Assembly	2
	2-Steel Shielding Assembly	37
	3-Steel Shielding Assembly	132
	4-Steel Shielding Assembly	223
	Boron Shielding Assembly	230
SA	Safety Rod Assembly	3
RE	Regulating Rod Assembly	2
SH	Shim Rod Assembly	3
	Neutron Source Assembly	1

Figure 2.2 CEFR Core radial configuration

Table 2.1 Main parameters of CEFR Core

Parameter	Value
Thermal/electric power, MW	65/20
Designed life, year	30
Maximum burn-up, MWd/t	60,000
Maximum neutron flux, $cm^{-2}s^{-1}$	3.2×10^{15}
Refueling period, day	80
Diameter/height of main vessel, m	8.0/12.2
Covering gas pressure, MPa	0.005
Core inlet/outlet temperature (full power), °C	360/530
SA lattice pitch, mm	61.0
SA outer/inner flat-to-flat dimension, mm	59.0/56.6
Wrapper thickness, mm	1.2

Table 2.2 Main Parameters of Subassemblies

	Fuel SA		Control SA		SS SA		Shielding SA
	Fuel	blanket	Regulating	Shim/safety	Type I&II	Type III&IV	
Number of SAs in core (operation loading)	79		2	3+3	39	355	230
Length of SA, mm	2592		2580		2592	2592	2592
Mass of SA, kg	29 - 31		22 - 23		41 - 43	42 - 44	31 - 33
Number of rods	61		7		7	1	7
Rod lattice pitch, mm	6.95		15.5		20.6	N/A	20.15
Outer diameter of rod/cladding, mm	6.00		14.9		20.0	54.0	19.2
Inner diameter of cladding, mm	5.40		12.9		N/A	N/A	17.2
Diameter of spacer wire, mm	0.95		1.3×0.6 [a)]		0.6	N/A	0.95
Screw pitch of spacer wire, mm	100		100		100	N/A	100
Effective material and enrichment, %	UO_2		B_4C		SS	SS	B_4C, Natural B
	64.4±0.5	0.3~0.72	Natural Boron	92.0% ^{10}B			
Total mass of UO2 or B_4C in each SA (kg)	5.30±0.13	1.28/3.23[b)]	0.87		N/A	N/A	2.43
Length of effective material, mm	450	100/250[b)]	510		N/A	N/A	800

a) The spacer wire is ellipse, and the major axis is 1.3mm and the minor axis 0.6mm
b) values upper and lower blankets, respectively.

Table 2.3 Expansion Coefficients

Material	Linear expansion coefficient
Fuel pellet	1.1×10^{-5}/°C
Blanket pellet	1.0×10^{-5}/°C
B_4C absorber	4.2×10^{-6}/°C
Stainless Steel	1.8×10^{-5}/°C

Table 2.4 Information of fuel rod

	Fuel	Blanket
Diameter of pellet, mm	5.20±0.15	5.20±0.15
Diameter of central hole, mm	1.6±0.1	N/A
Design value of pellet density, g/cm^3	10.5±0.2	≥10.3
Oxygen-to-metal (O/M) ratio	2.000~2.015	2.000~2.015
Pressure of helium gas, MPa	2.6	

Table 2.5 Total mass of fuel/blanket in each fuel SA

		Average	Standard Deviation	Minimum	Maximum
Fuel	Mass of UO2, kg	5.28127	0.01295	5.2570	5.3421
	Mass of U, kg	4.64602	0.01167	4.6246	4.6979
	Mass of U-235, kg	2.98197	0.00852	2.9667	3.0156
	U Enrichment, %	64.18315	0.09761	64.08	64.41
Blanket	Mass of UO2, kg	4.56629	0.01548	4.5345	4.6079
	Mass of U, kg	4.01855	0.01418	3.9940	4.0587
	Mass of U-235, kg	0.0179	3.1403E-4	0.0172	0.0183
	U Enrichment, %	0.44532	0.00719	0.42924	0.45646

Table 2.6 Total mass of absorber in each control SA

		Design Value	Measured value				
			Average	Standard Deviation	Minimum	Maximum	Total Number
Mass of B4C, kg		0.87±0.07	0.86545	0.00522	0.86	0.87	11
Mass of B-10, kg	Shim & Safety SAs	0.59±0.05	0.58625	0.00518	0.58	0.59	8
	Regulating SAs	0.119±0.04	0.11733	5.7735E-4	0.117	0.118	3

Table 2.7 Neutron Detectors in CEFR

		Number	Type	Distance from core center, mm
Physical Startup	Dedicated for start-up	3	^{235}U fission chamber	(r)1600 (h)1050
Outer core detectors	Source range	4	Lining ^{10}B proportional counter	(r)5747
	Intermediate range	6	^{235}U fission chamber	(r)6047
	Power measurement	2	γ-ionization chamber	(r)7447
	Power protection	6	γ – ionization chamber	(r)6502
	Period protection	6	γ – ionization chamber	(r)7447

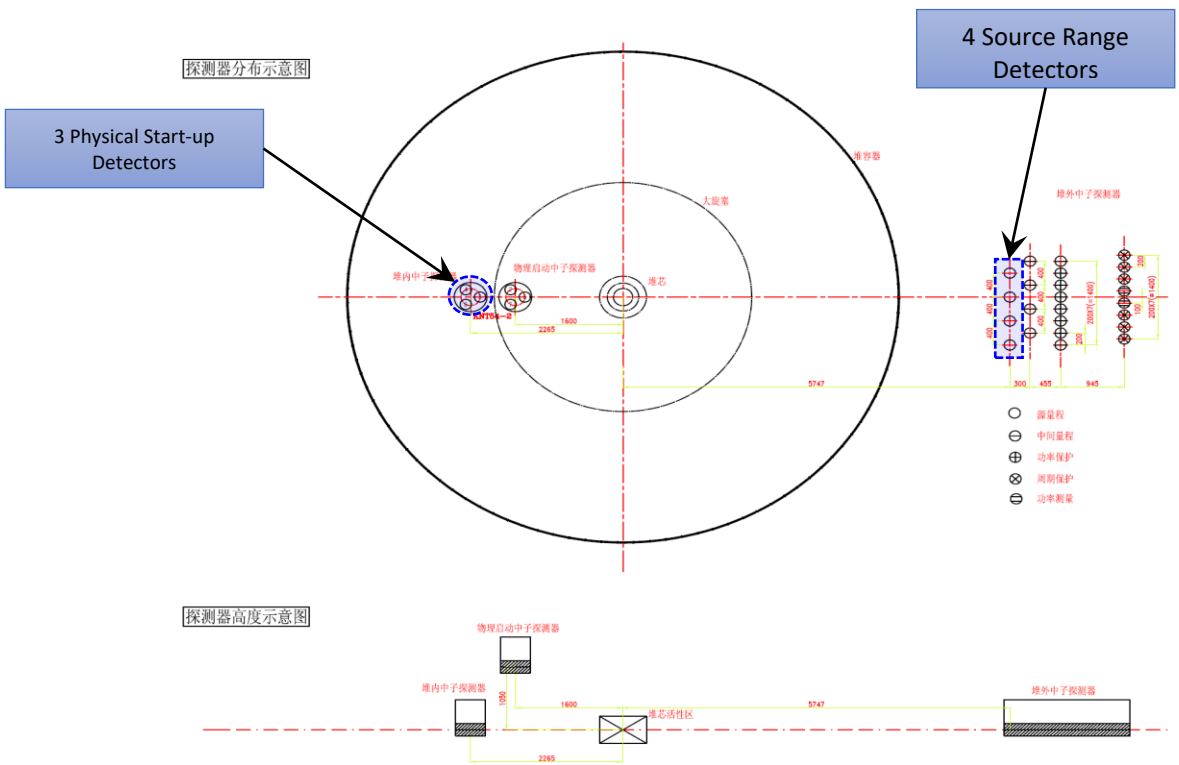

Figure 2.3 Locations of start-up detectors and source-range detectors

3. CEFR Model and Calculation Methodologies

The neutron flux distribution in the CEFR core was calculated using the variational nodal code, DIF3D-VARIANT, that can solve spherical harmonics P_n transport equation. In this benchmark, P_3 or P_5 angular expansion approximation of the scattering source and flux and a P_1 expansion approximation for the leakage between nodes were adopted, along with 4th, 6th and 1st -th order polynomials in space for the flux, source, and leakage approximations. The region dependent 33-group cross sections are generated using a standard two-step MC^2-3/TWODANT process (Lee et al., 2015 and Alcouffe et al., 1984) with the ENDF/B-VII nuclear data library.

The details of the core modeling approximations and cross section generation are given in the report from the blind benchmark (Jarrett et al. 2019). No significant changes were made, but some of the non-fuel regions were refined in the open benchmark. These updates to the model are covered in this section.

3.1 Fuel subassembly Model

The most significant update to the fuel subassembly model is that the active core was divided into two radial regions (inner and outer) for the purpose of generating multigroup cross sections. In the blind phase, the same cross sections were used for all driver regions. In the updated model, the outer two rows of fuel assemblies are separated from the inner fuel assemblies and have their own cross sections calculated by condensing with the local flux spectrum in the outer fuel region. The updated TWODANT 2D R-Z geometry is shown in Figure 3.1. In the actual model there are more regions than can be easily displayed with the discrete colormap in Figure 3.1; many of the less important regions are condensed into a single region for this figure, such as “reflector” or “connecting.” Other modifications, which are likely less impactful, are listed below:

- The “lower connector” region of the fuel (bottom 8.7 cm) was changed from the “connecting_I” material (steel/sodium blend from Version 3 of benchmark) to a steel duct full of sodium coolant.
- The duct material in fuel assemblies was changed from “fuel_steel” (7.97 g/cc) to “structure” (7.98 g/cc). These two steels have mostly identical compositions, except for small differences in the concentration of various alloy and minor constituents, including Si, C, Mo, Ni, Mn, and Ti. Only the cladding and wire wrap are composed of the fuel steel material. The compositions are given in Table 3.1. The Si, Ti, and C were not included in the blind phase model since they are minor constituents.
- The region directly above the upper blanket was previously called “fuel connecting,” composed of the connecting-I material from the previous benchmark version. This 12.5 cm region represented the fuel spring (4.5 cm), top end plug (2.0 cm), and upper plenum (6.0 cm). In the new model, the fuel spring and top end plug are combined into a single region that is modeled as the springs (empty cladding), and the upper plenum is modeled as sodium-filled duct.

- The upper reflector region of the fuel (top 23 cm) was previously modeled with the "handling head" composition from version 3 of the benchmark. The material was updated to a 35.5% steel volume fraction, consistent with the drawings provided in benchmark version 7.

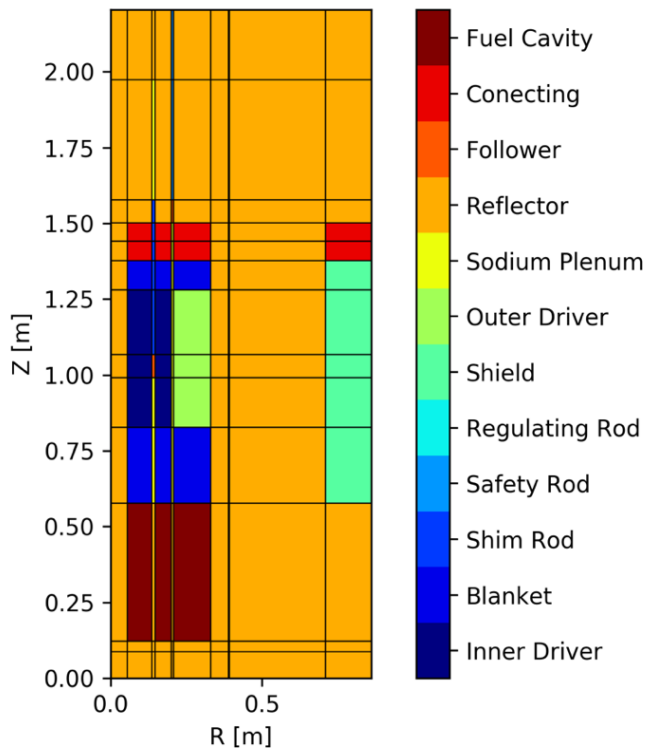

Figure 3.1 TWODANT 2D R-Z geometry for ultra-fine group spectrum calculation

Table 3.1 Steel composition (mass fraction) for fuel and structural steels

	Fuel Steel (Cladding and Wire Wrap)		Structural Steel	
	FY20	FY19	FY20	FY19
Fe	64.44%	65.30%	65.19%	66.25%
Ni	14.75%	14.75%	12.50%	12.50%
Cr	16.25%	16.25%	17.00%	17.00%
Mo	2.20%	2.20%	2.50%	2.50%
Mn	1.50%	1.50%	1.75%	1.75%
Ti	0.35%	0.00%	0.40%	0.00%
Si	0.45%	0.00%	0.60%	0.00%
C	0.06%	0.00%	0.06%	0.00%

3.2 Control subassembly Model

In the updated model, there were a few updates to the control assemblies.

- The control rod follower region (7.4 cm) was divided into the follower (3.2 cm) and the baffle (4.2 cm); the baffle has a lower steel volume fraction than the follower.
- The lower shielding region (65 cm) was changed from the “reflector-II” material from version 3 of the benchmark to a similar but more precise composition of 73.4% steel. by volume.
- The plenum (3.1 cm) directly above the control rod, and the upper connector (6.5 cm) directly above the plenum, were not explicitly modeled in the previous version. In the updated model, these two regions are combined (9.6 cm total), and the region is treated as 33.3% steel by volume, which is the specification for the upper connector given in the design drawings of the control rod.
- The region directly above the upper connector is the upper plenum/control rod shaft. It was previously modeled as the “gas cavity” material from version 3 of the benchmark, which is a mixture of sodium and steel, diluted by the “void” space inside pins. In the updated model, it is given a steel volume fraction of 31.1%, consistent with the design drawings.
- The head connector (8.9 cm), handling head (7.8 cm), and gripper (5.1 cm) were previously modeled as a single 23 cm region with the handling head material. The updated model still uses the approximate length of 23 cm (instead of 21.8 cm) in order to line up with the fuel subassembly model, but the steel volume fraction of 28.4% is more consistent with the design drawing.

3.3 Reflector subassembly Model

The reflector assemblies were not modified in the updated version of the benchmark. These assemblies are relatively simply geometrically and were already modeled at the level of detail given in the design drawings. However, a large error was observed when calculating the Au-197 (n,γ) reaction rate in the radial reflector. Thus, in the further investigation, the experimental subassemblies in the radial reflector was refined to capture the spatial self-shielding effect (see Section 6).

3.4 Shield subassembly Model

The shield assemblies are placed relatively far from the active core, so small details in these assemblies are less important to obtaining accurate neutronics solutions. As a result, the model of the shield subassembly was adjusted to fit the axial mesh from the rest of the problem to avoid having new axial mesh positions introduced for the shield. Extra axial planes like this can create small axial regions, especially with moving control rods, which can cause DIF3D-VARIANT to fail to converge. The modifications are listed below:

- The lower reflector region of the shield (50.6 cm) was combined with the plena (1.8 cm and 2.0 cm) and the "lower structure" (2.8 cm); the combined region is given the composition of the lower reflector, which is 73.4% steel by volume.
- The absorber region was reduced from 86.5 cm to the correct value of 80.0 cm. The other 6.5 cm were modeled as a separate region with a steel volume fraction of 48.9%.
- The upper reflector region (78.5% steel), which is actually 47.5 cm tall, is modeled as 53.0 cm to align with the fuel subassembly mesh.
- The "head" region, which is actually 27.0 cm tall, is modeled as 23.0 cm to align with the fuel subassembly mesh. The steel volume fraction is 44.9%.

3.5 Mock Fuel subassembly Models

The mock fuel subassembly is used in the approach to criticality. It is important for the initial critical configuration because there are seven mock fuel assemblies loaded into peripheral fuel subassembly locations. The modifications to this subassembly model are listed below:

- The 27.8 cm filter region of the mock assemblies, which overlaps with the top 13.4 cm of the driver fuel region, was previously modeled with void inside of the filter region. In the updated model, this inner region is instead filled with sodium, which is correct.
- The plenum region (8.1 cm) above the filter was previously modeled as the connecting-I material. In the updated model, it is a sodium-filled steel duct.
- The handling head region was changed from the "handling_head" material to the explicit model, with a steel volume fraction of 44.9%.

3.6 Summary of Changes

Most of these modifications from the blind phase of benchmark to the open phase of benchmark are effectively small changes to the relative number densities of steel and sodium.

In an earlier version of the benchmark technical specifications (version 5, Hue 2018), the homogenized number densities for each region were given directly using the nominal design values. The models for the blind phase of benchmark were originally developed with these given compositions. Detailed drawings of various subassemblies were given in the final version of the technical specifications (version 6, Huo 2019). These drawings could be used to calculate precise number densities of steel and sodium for the homogenized subassembly model.

In the open phase of the benchmark, all these regions were given updated material compositions to rule out the possibility of these slight modeling errors contributing to discrepancies between the model results and the measured data. Most of these changes will have little effect on the results, especially those to regions far from the active core (handling head, lower reflector, shield assemblies). The changes to control rod connector, follower, and baffle may slightly impact control rod worth. The changes to the mock fuel subassembly could affect the approach to criticality. The most significant change is the separate the active core into inner and outer core regions in the cross-section generation.

4. Benchmark Comparison to Experimental Measurements

Start-up tests were performed in the zero power of CEFR to measure various reactor physics parameters that are needed for operation reactor safely and validation of computation codes. Some of these experimental measurements were selected for the CRP, which are:

1. criticality per fuel subassembly loading,
2. control rod worth,
3. sodium void worth,
4. temperature reactivity coefficient,
5. sub-assembly exchange reactivity change,
6. reaction rate distribution measured with activation foils.

4.1 Approach to criticality per loading of fuel subassemblies

The initial approach to criticality was performed at the cold state to determine the number of fuel subassemblies required for the CEFR core to be critical without shim rods inserted. In the benchmark specification, the cold state indicates that the average coolant temperature is 250°C. The startup loading is shown in Figure 4.1.

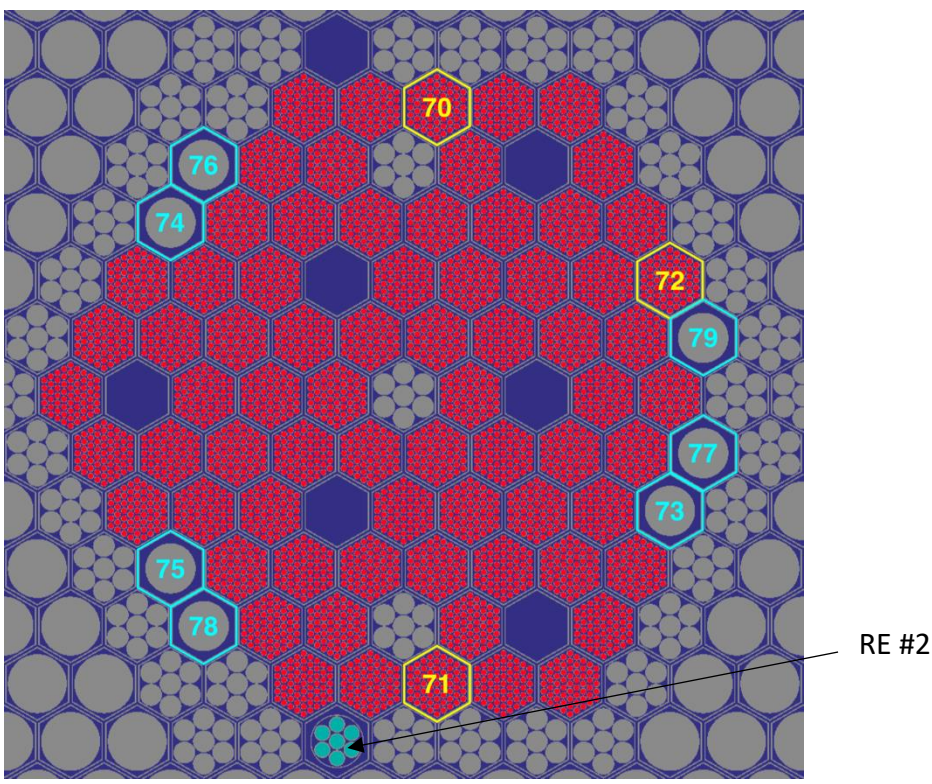

Figure 4.1. Core configuration for approach to criticality

In the very beginning, 79 locations (red subassemblies and numbered from 70 to 79 in Figure 4.1) are loaded with mock-up subassemblies, and the mock-up subassemblies were replaced by fuel subassemblies one-by-one from the core center to periphery. The core approached to a near critical state when 72 mock-up subassemblies were replaced by fuel subassemblies. Finally, the criticality state was achieved by adjusting the axial position of the regulating rod (RE) #2. CIAE measured the criticality using a neutron count inverse extrapolation method. The reactivity measurement uncertainty was about 5 pcm in the experiment.

This experiment was modeled using the DIF3D-VARIANT code using the 4th, 6th and 1st order polynomials of source, flux, leakage spatial expansion approximations. The measured values and calculation results are provided in Table 4.1. The evaluated core criticality by the DIF3D-VARIANT code is about 110 pcm lower than the measured value.

Table 4.1 Approach to criticality at 250°C

Fuel Assemblies Inserted	RE2 Control Rod Position (mm)	Other rods Position (out from active core)	Measurement [a)]	Evaluation by ARC code
70	500	500	-	0.99166
71	500	500	-	0.99588
72	190	500	1.00040	0.99933
72	170	500	1.00034	0.99925
72	151	500	1.00025	0.99916
72	70	500	1.00000	0.99890

a) Measurement uncertainty is ±5 pcm.

The core multiplication factors evaluated by participants are compared in Figure 4.2. The used computation codes and neutron libraries by participants are provided in Appendix A. For comparison purpose, the results from deterministic and stochastic codes are colored differently (blue: deterministic, orange: stochastic). Except for several outliers (> 500 pcm), the results from deterministic and stochastic codes are generally comparable, and the predicted criticalities are within a few hundred pcm from the measured value. The outliers were due to the misunderstanding of the criticality measurement or inaccurate cross sections.

It is noted that the results from participants are different even though they used the same reactor analysis codes. For instance, several participants used the DIF3D and Serpent codes for deterministic and stochastic calculations, respectively. However, as shown in Figure 4.2, the results are different depending on the neutron libraries, cross sections generation methods, and modeling of the core. This observation informs that experiences of fast reactor analyses and knowledge on computation codes are important factors to have accurate results.

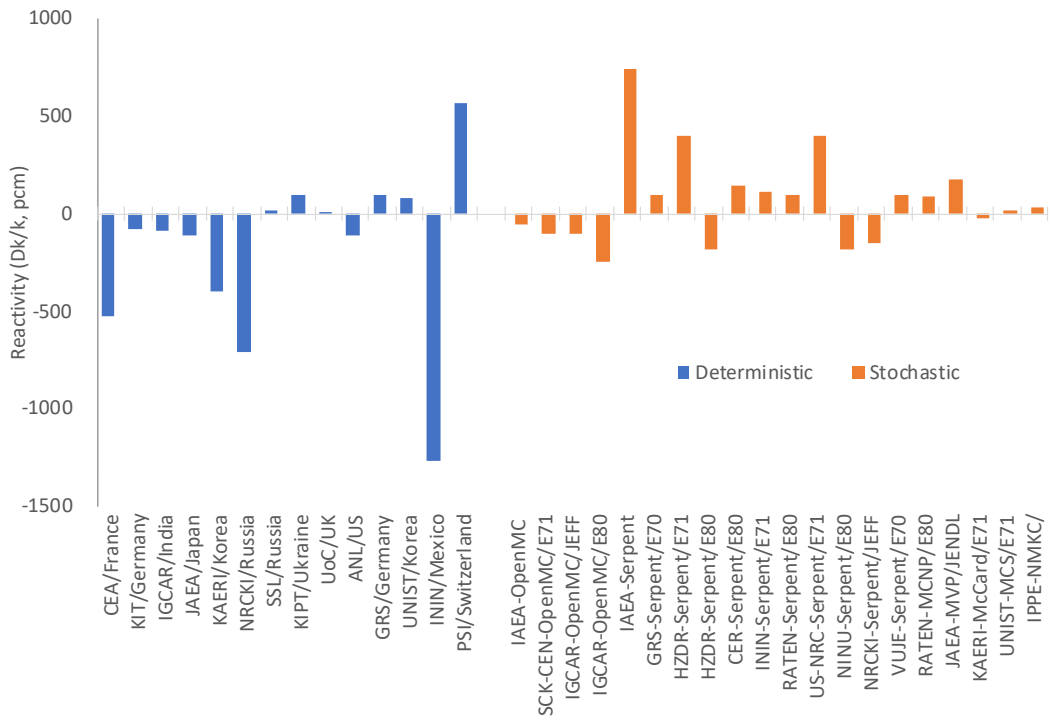

Figure 4.2 Prediction of criticality by participants

4.2 Control rod worth measurements

The control rod worth was measured in the basic core layout at cold state. The basic core layout is shown in Figure 4.3, which consists of 79 fuel subassemblies. From the initial critical core layout (see Figure 4.1) with 72 fuel subassemblies, the basic core layout was developed by loading additional seven fuel subassemblies. For compensation of the extra reactivity insertion with the seven fuel subassemblies, the shim and regulating control rods were inserted in the basic core layout.

In the experiment, the control rod worth was measured using an inverse kinetics and period method by dropping control rods or inserting control rod with nominal speed of movement. Fourteen cases of control rod worth were measured. The control rods positions before and after movements of control rods are given

The calculated control rod worth values are compared to the measured data in Table 4.3. The differences between the calculated values and measured values are provided in the last column of the table. The results are generally close to the measured values. Among the total 14 cases, the calculated control rod worth values are within one standard deviation of the measured errors. DIF3D-VARIANT overestimated the control rod bank work for the case of the 1st shutdown system with one-rod stuck (highlighted in yellow). The difference is more than two standard deviations of the measured error.

Most of the experiments involve a complete rod drop, from full withdrawal to full insertion. The resulting change in reactivity is the total worth of that rod or bank of rods. In some cases, the rod drop begins from a position of partial insertion, so the rod worth reported is not the full worth from 0 to 100% insertion. The full-insertion worth of each control rod subassembly and bank with all other control assemblies withdrawn is given in Table 4.4. This was not a real experiment, but it is a useful model and is part of the benchmark work package. The integral rod worth for each individual rod is given in

Table 4.5, and the differential worth is given in

Table 4.6. The integral worth is plotted in Figure 4.4. The full stroke for the integral rod worth goes from the bottom of the driver fuel region to 50 mm above the top of the driver region. The rod worth is defined as 0 at 500 mm withdrawn, which is where the bottom of the absorber pins is 50 mm above the top of the driver fuel region, in the upper blanket region.

Table 4.2, including the measured control rod worth and measurement errors. The shim bank and safety bank have greater worth and measurement errors than those of the regulating rods because both rods use enriched B_4C (92 at% B-10) and are located within the active core.

The control rod worth was calculated by comparing the core multiplication factors before and after movement of control rods. In the DIF3D-VARIANT calculations, the core was divided into axial nodes depending on the materials and power distributions, but the number of axial nodes cannot be increased until an axial mesh is exactly matched with the control rod locations because a tiny axial node size causes an instability issue in the DIF3D-VARIANT calculations. So, the rod axial locations are rounded to the nearest axial nodes and the k-effective values are corrected at the exact position using a linear interpolation of two rod worth values.

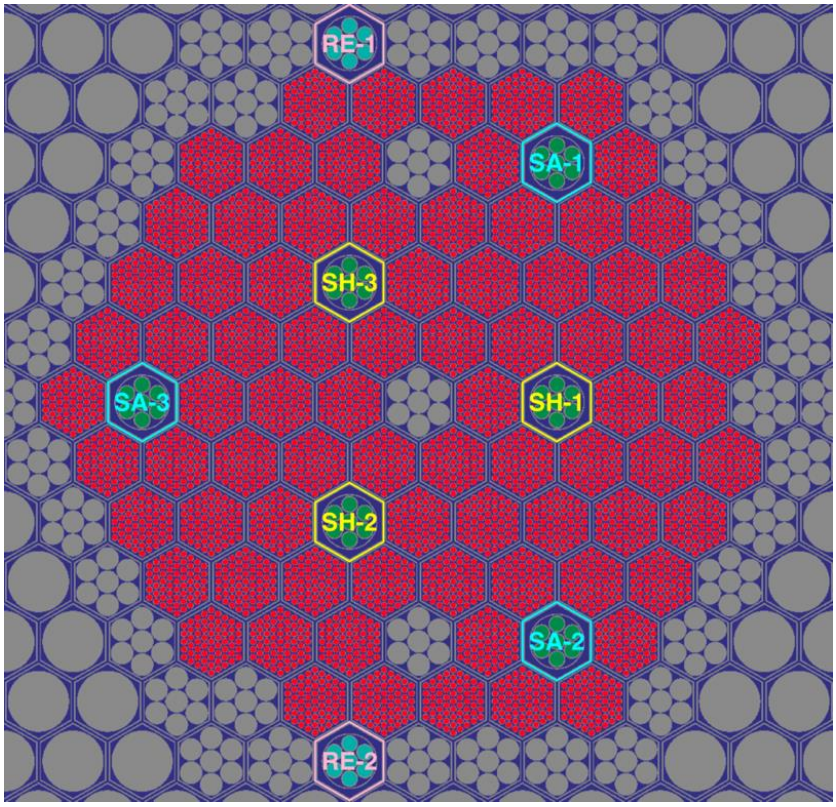

Figure 4.3. CEFR basic core layout for control worth measurement

The calculated control rod worth values are compared to the measured data in Table 4.3. The differences between the calculated values and measured values are provided in the last column of the table. The results are generally close to the measured values. Among the total 14 cases, the calculated control rod worth values are within one standard deviation of the measured errors. DIF3D-VARIANT overestimated the control rod bank work for the case of the 1st shutdown system with one-rod stuck (highlighted in yellow). The difference is more than two standard deviations of the measured error.

Most of the experiments involve a complete rod drop, from full withdrawal to full insertion. The resulting change in reactivity is the total worth of that rod or bank of rods. In some cases, the rod drop begins from a position of partial insertion, so the rod worth reported is not the full worth from 0 to 100% insertion. The full-insertion worth of each control rod subassembly and bank with all other control assemblies withdrawn is given in Table 4.4. This was not a real experiment, but it is a useful model and is part of the benchmark work package. The integral rod worth for each individual rod is given in

Table 4.5, and the differential worth is given in

Table 4.6. The integral worth is plotted in Figure 4.4. The full stroke for the integral rod worth goes from the bottom of the driver fuel region to 50 mm above the top of the driver region. The

rod worth is defined as 0 at 500 mm withdrawn, which is where the bottom of the absorber pins is 50 mm above the top of the driver fuel region, in the upper blanket region.

Table 4.2 Control rod worth measurement

Rod Bank	Rod or rod group		Control rod positions/mm								Rod worth, pcm	
			RE1	RE2	SH1	SH2	SH3	SA1	SA2	SA3	Value	**error**
Regulating	RE1	Before	501	106	240	240	239	498	500	500	150	±9
		After	-1	106	240	240	239	498	500	500		
	RE2	Before	106	499	240	240	239	498	500	500	149	±9
		After	106	5	240	240	239	498	500	500		
Shim rod	SH1	Before	240	240	501	141	141	498	499	499	2019	±250
		After	240	240	4	141	141	498	499	499		
	SH2	Before	239	240	151	498	151	498	500	500	1839	±225
		After	239	240	151	-1	151	498	500	500		
	SH3	Before	240	239	148	150	498	498	500	500	1839	±226
		After	240	239	148	150	7	498	500	500		
Safety rod	SA1	Before	240	239	240	240	241	498	499	499	945	±100
		After	240	239	240	240	241	46	499	499		
	SA2	Before	240	240	240	240	240	498	499	499	911	±100
		After	240	239	240	240	240	498	55	499		
	SA3	Before	240	239	240	240	240	498	499	499	946	±98
		After	240	239	240	240	240	498	499	40		
1st shutdown system	3*SH+ 2*RE	Before	247	247	239	240	239	498	500	499	2877	±355
		After	0	5	1	-1	7	498	500	499		
1st shutdown system with SH1 stuck	SH2+SH3+2*RE	Before	247	248	501	141	141	498	500	499	881	±76
		After	-2	2	501	-3	16	498	500	499		
2nd shutdown system	3*SA	Before	247	249	240	240	240	498	500	499	2981	±395
		After	247	249	240	240	240	46	56	40		
2nd shutdown system with SA3 stuck	SA1+SA2	Before	247	248	240	240	240	498	500	500	1950	±226
		After	247	248	240	240	240	45	54	500		
All control rods	2*RE+ 3*SH+ 3*SA	Before	247	248	240	240	240	499	500	500	6079	±989
		After	0	3	2	-2	0	45	56	40		
All control rods with SH1 stuck	2*RE+ SH2+SH3+3*SA	Before	248	248	500	141	141	498	500	499	3899	±551
		After	-2	2	500	-3	7	45	55	40		

Table 4.3 Comparison of calculated control rod worth with measurement

Rod Bank	Rod Group	Measured rod worth, pcm		Evaluated rod worth, pcm	
		Value	Error	Value	Diff. from measured
Regulating	RE1	150	±9	-144.8	-5
	RE2	150	±9	-143.9	-5
Shim rod	SH1	2019	±250	-1902.8	-116
	SH2	1839	±225	-1852.1	13
	SH3	1839	±250	-1852.1	13
Safety rod	SA1	945	±100	-1024.5	79
	SA2	911	±225	-1006.3	95
	SA3	946	±98	-1080.4	134
1st shutdown system	3*SH+2*RE	2877	±226	-3017.2	140
1st shutdown system with SH1 stuck	SH2+SH3+2*RE	881	±76	-1095.0	214
2nd shutdown system	3*SA	2981	±100	-2948.5	-32
2nd shutdown system with SA3 stuck	SA1+SA2	1950	±226	-1777.7	-172
All control rods	2*RE+ 3*SH+ 3*SA	6079	±100	-6101.6	23
All control rods with SH1 stuck	2*RE+ SH2+SH3+3*SA	3899	±551	-3978.3	79

Table 4.4 Control rod worth of individual subassembly and banks for full insertion

Rod Bank	Rod or rod group	Control rod positions, mm								Evaluated worth	
		RE1	RE2	SH1	SH2	SH3	SA1	SA2	SA3	k-eff	worth
All control rods out of core	2*RE+ *SH+ 3*SA	500	500	500	500	500	500	500	500	1.02972	-
Regulating rod worth	RE1	0	500	500	500	500	500	500	500	1.02820	-143
	RE2	500	0	500	500	500	500	500	500	1.02820	-143
	2*RE	0	0	500	500	500	500	500	500	1.02664	-291
Shim rod worth	SH1	500	500	0	500	500	500	500	500	1.01098	-1800
	SH2	500	500	500	0	500	500	500	500	1.01137	-1762
	SH3	500	500	500	500	0	500	500	500	1.01137	-1762
	3*SH	500	500	0	0	0	500	500	500	0.97422	-5532
Safety rod worth	SA1	500	500	500	500	500	0	500	500	1.01974	-951
	SA2	500	500	500	500	500	500	0	500	1.01975	-949
	SA3	500	500	500	500	500	500	500	0	1.01937	-986
Worth of 1st shutdown system	3*SH+ 2*RE	0	0	0	0	0	500	500	500	0.97121	-5851
Worth of 1st shutdown system with SH1 stuck	SH2+SH1 +2*RE	0	0	500	0	0	500	500	500	0.99002	-3894
Worth of 2nd shutdown system	3*SA	500	500	500	500	500	0	0	0	0.99837	-3049
Worth of 2nd shutdown system with SA3 stuck	SA1+SA2	500	500	500	500	500	0	0	500	1.00943	-1952
All control rods	2*RE+ 3*SH + 3*SA	0	0	0	0	0	0	0	0	0.94184	-9061
All control rods with SH1 stuck	2*RE+ SH2+ SH3+ 3*SA	0	0	500	0	0	0	0	0	0.96015	-7036

Table 4.5 Integral worth for each rod at 50 mm intervals

Control rod positions, mm	ρ_I, pcm							
	RE1	RE2	SH1	SH2	SH3	SA1	SA2	SA3
500	0	0	0	0	0	0	0	0
450	-7	-7	-84	-83	-83	-43	-43	-44
400	-19	-19	-235	-230	-230	-121	-120	-124
350	-34	-35	-442	-433	-433	-226	-226	-234
300	-55	-55	-690	-676	-676	-355	-355	-369
250	-74	-74	-950	-930	-930	-490	-489	-508
200	-94	-94	-1201	-1175	-1175	-622	-621	-645
150	-112	-112	-1423	-1393	-1393	-740	-739	-769
100	-126	-126	-1600	-1566	-1566	-837	-836	-868
50	-138	-138	-1733	-1696	-1696	-912	-910	-946
0	-143	-143	-1800	-1762	-1762	-951	-949	-986

Table 4.6 Differential worth for each rod at 50 mm intervals

Control rod positions, mm	ρ_D, pcm/mm							
	RE1	RE2	SH1	SH2	SH3	SA1	SA2	SA3
475	0.15	0.15	1.68	1.65	1.65	0.86	0.86	0.89
425	0.23	0.23	3.02	2.95	2.95	1.55	1.54	1.59
375	0.31	0.31	4.13	4.06	4.06	2.12	2.11	2.20
325	0.40	0.40	4.97	4.86	4.86	2.58	2.58	2.69
275	0.39	0.39	5.21	5.09	5.09	2.69	2.69	2.79
225	0.39	0.39	5.01	4.90	4.90	2.64	2.64	2.74
175	0.36	0.36	4.45	4.35	4.35	2.36	2.36	2.47
125	0.28	0.28	3.54	3.46	3.46	1.93	1.93	1.99
75	0.25	0.23	2.66	2.61	2.60	1.50	1.48	1.55
25	0.10	0.11	1.34	1.31	1.32	0.78	0.79	0.80

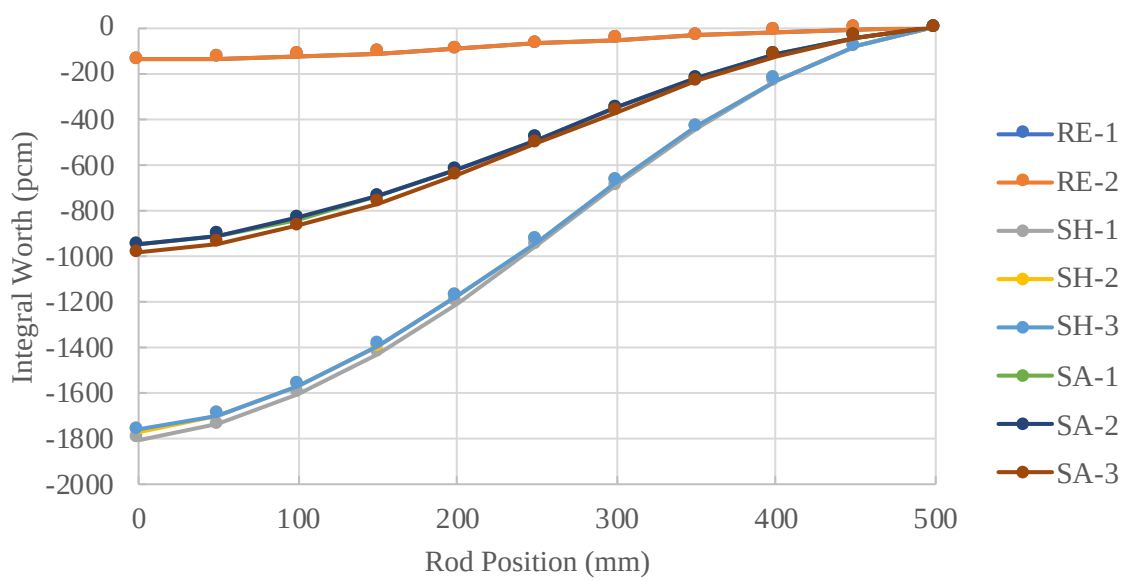

Figure 4.4 Integral worth for each control subassembly

4.3 Sodium void reactivity worth

The sodium void worth was measured by replacing a single fuel subassembly with a voided experimental fuel subassembly. The voided experimental fuel subassembly is identical to the fuel subassembly, but the coolant inlet holes was blocked. Thus, the sodium coolant cannot flow into the duct of the experimental fuel subassembly, and as a result, there is no sodium inside the duct (i.e., voided).

The locations where voided assemblies were placed are shown in Figure 4.5. In the experiment, the regulating rods were moved to achieve the criticality at the original and the voided cases. Then, the different locations of regulating rods were converted into the reactivity change between the original and voided cases. For the DIF3D-VARIANT model, however, the control rods are kept in the same position, and the sodium void worth was calculated by comparing the k-effective differences between the original and voided cases. The resulting sodium void worth is reported in Table 4.7.

The sodium void reactivity worth is dependent on the neutron importance in the core: i.e., the sodium void worth is high in the core center and core region with higher fissile content and low in the core periphery. The evaluated sodium void worth is slightly more negative than the measured values. Except for the case at position #5 (core periphery), the calculated values are agreed with the measured values within the one standard deviation of the measurement errors.

The average sodium void worth of five locations was compared with the values calculated by participants in Figure 4.6. The average values were compiled by computation methods of participant's codes. Generally, the deterministic codes, including ANL code, estimated the sodium void worth more negative compared to the measured value, while the stochastic codes estimated the sodium void worth less negative.

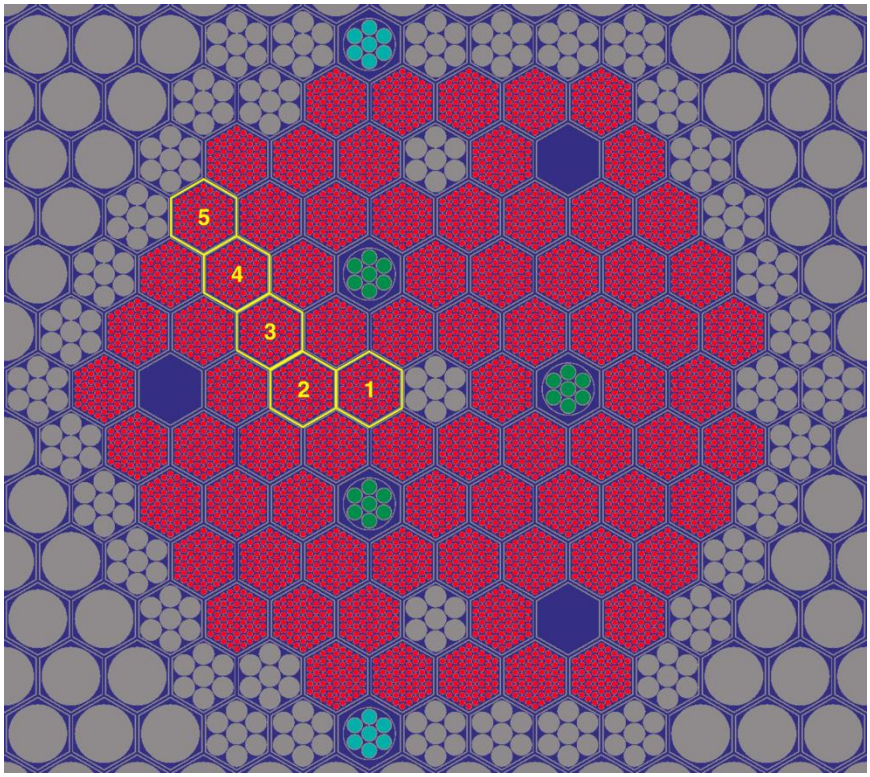

Figure 4.5 subassembly locations for sodium void measurements

Table 4.7 Voided subassembly experiment, no control rod movement

Measurement position in core		Control rod positions		Temp (°C)	FY20		Measurement	
		RE1	RE2		k-eff	Void Worth	Void Worth	error
#1 (2-4)	Original	277	277	250	0.99891	-44.1	-39.2	±5.8
	Voided	277	277	250	0.99847			
#2 (3-7)	Original	277	277	250	0.99891	-45.1	-43.4	±5.9
	Voided	277	277	250	0.99846			
#3 (4-9)	Original	277	277	250	0.99891	-44.1	-40.5	±5.7
	Voided	277	277	250	0.99847			
#4 (5-11)	Original	277	277	250	0.99891	-43.1	-40.1	±5.5
	Voided	277	277	250	0.99848			
#5 (6-13)	Original	277	277	250	0.99891	-43.1	-32.9	±5.5
	Voided	277	277	250	0.99848			

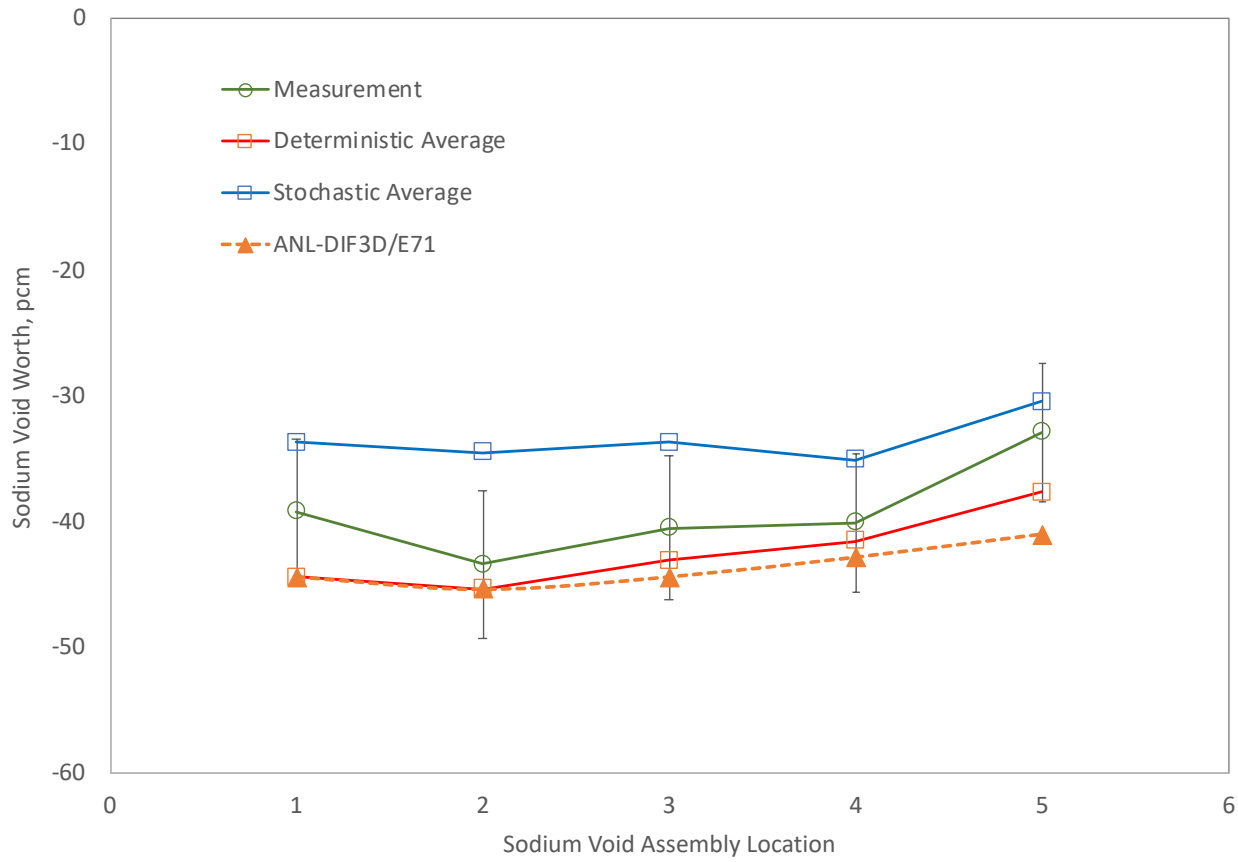

Figure 4.6 Comparison of sodium void worth

4.4 Temperature reactivity coefficient

The reactivity change per the average coolant temperature was measured at five temperature levels by increasing temperatures from 250 to 300 °C and decreasing the temperatures from 300 to 250 °C. The experiments were conducted based on following procedures:

- At shutdown state the coolant temperature of reactor core was changed to a certain value and kept the state for at least half an hour,
- Search control rod locations where the core became critical,
- Difference of control rod locations from the critical control rod location at 250 °C (for increasing case) or 300 °C (for decreasing case) gave the reactivity change,
- Control rods were then inserted for shutting down reactor,
- Temperature was changed to the next level and repeated the previous steps.

About 14 thermal couples were installed above the reactor core to get the average outlet coolant temperature of sodium, which was regarded as the uniform temperature of whole core. The temperature changes and measured reactivity coefficients are given in Table 4.8. The

reactivity coefficients are different between the temperature increasing and decreasing cases even though the temperature coefficients are expected to be identical regardless of the increasing or decreasing temperature. For instance, the measured temperature reactivity coefficient was 3.88 pcm/K when increasing temperature from 250 °C to 302 °C, while it was -4.39 pcm/K when decreasing temperature from 300 °C to 250 °C. The different temperature coefficients between the increasing and decreasing cases are due to experimental method to search the critical positions using the inverse kinetics method and the period method: i.e., slightly positive reactivity was measured for the temperature increasing case, while slightly negative reactivity was measured for the temperature decreasing case.

Table 4.8 Measurement data of temperature reactivity coefficient

Condition	Temperature, °C	Coefficient, pcm/°C	Measurement error,
Temperature increasing progress	250		
	274	-3.78	±0.55
	283	-3.52	±0.49
	293	-3.54	±0.47
	302	-3.88	±0.52
Temperature decreasing progress	300		
	290	-4.46	±0.73
	280	-4.05	±0.58
	270	-4.31	±0.58
	250	-4.39	±0.58

In the DIF3D-VARIANT model, the temperature reactivity coefficients were calculated by the k-effective values at different temperature levels without changing the control rod locations. The cross-section sets at five temperature levels were generated. The calculated temperature coefficients are given in Table 4.9. The average temperature reactivity coefficient in the coolant temperature interval of 250 – 300 °C is approximately -4.3 pcm/K, which is close to the measured temperature reactivity coefficient in the temperature decreasing case.

Table 4.9 Temperature reactivity coefficient

Temp (°C)	Control rod positions (mm)		k-eff	Coefficient (pcm/°C)
	Regulating	Shim		
250	229	240	0.99891	
275	229	240	0.99769	-4.9
283	229	240	0.99735	-4.3
293	229	240	0.99686	-4.9
302	229	240	0.99648	-4.3

In Figure 4.7, the average temperature reactivity coefficient in the temperature interval of 250 °C and 300 °C was compared with the results calculated by several participants. The measured temperature coefficient is the average value of the increasing temperature case and the decreasing temperature case. Temperature reactivity coefficients from deterministic codes are

generally agreed with the measured value within one-standard deviation of the measurement error, while temperature reactivity coefficients from stochastic codes are somewhat less negative compared to the measured value.

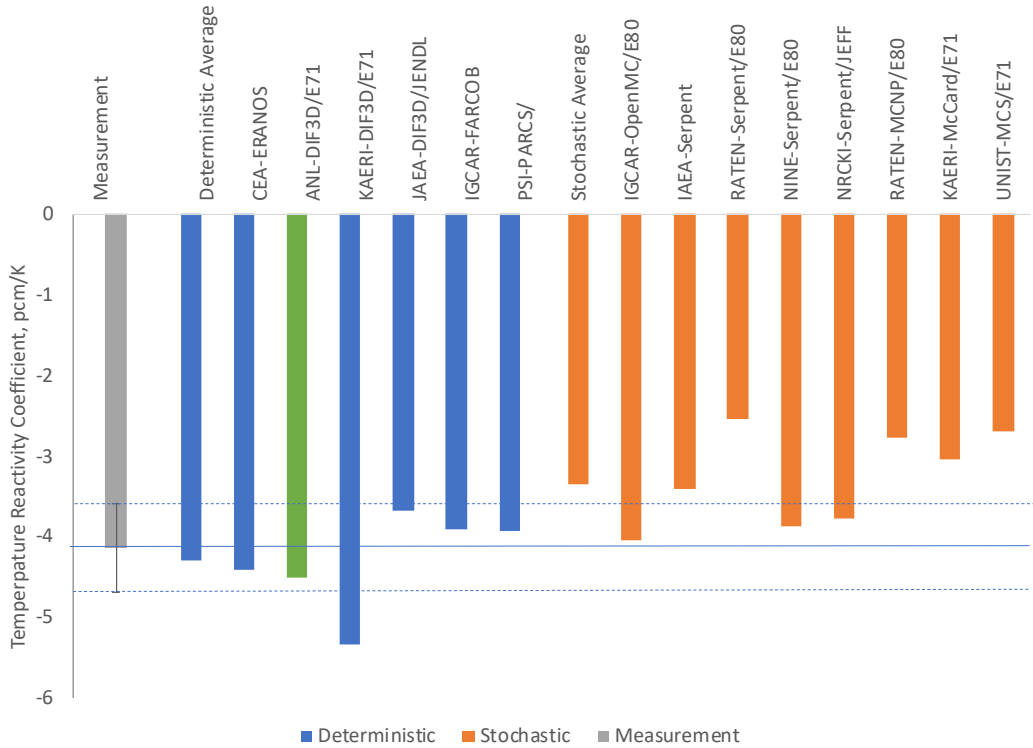

Figure 4.7 Comparison of temperature reactivity coefficient

4.5 Subassembly swap reactivity

The subassembly swap reactivity measurement was an experiment where a subassembly in the core was swapped for another one, and the change in reactivity was measured. This experiment was conducted to assess the possible accident of fuel loading error. The locations of subassemblies that are swapped are shown in Figure 4.8. Fuel subassemblies (locations from #1 to #6) were replaced by the SS Type-I subassembly (see composition in Table 2.2), which is a reflector subassembly. The location #7 (reflector) was replaced by a fuel subassembly, and the location #8 (control rod) was replaced by the SS Type-I subassembly.

In the experiment, the swap reactivity was calculated using the change of critical control rod positions between the original core configuration and the swap core configuration. However, in the DIF3D-VAIANT calculations, the swap reactivities were calculated using the k-effective change the original core configuration and the swap core configuration. The measured values and calculation results of the subassembly swap experiment are given in

Table 4.10. The measurement error was ±13%. In Figure 4.9, the results are compared with the average values of deterministic and stochastic calculations by participants.

The calculated swap reactivities are less negative than the measured values within one standard deviation of measurement error. The results of most participants are also less negative than the measured values. A potential reason of the common underestimations by participants is the different reactivity calculation methods between calculations and measurements: i.e., participants calculated the swap reactivity using different eigenvalues without changing the control rod positions, while experiment measured the change of critical control rods positions and converted it into the reactivity change.

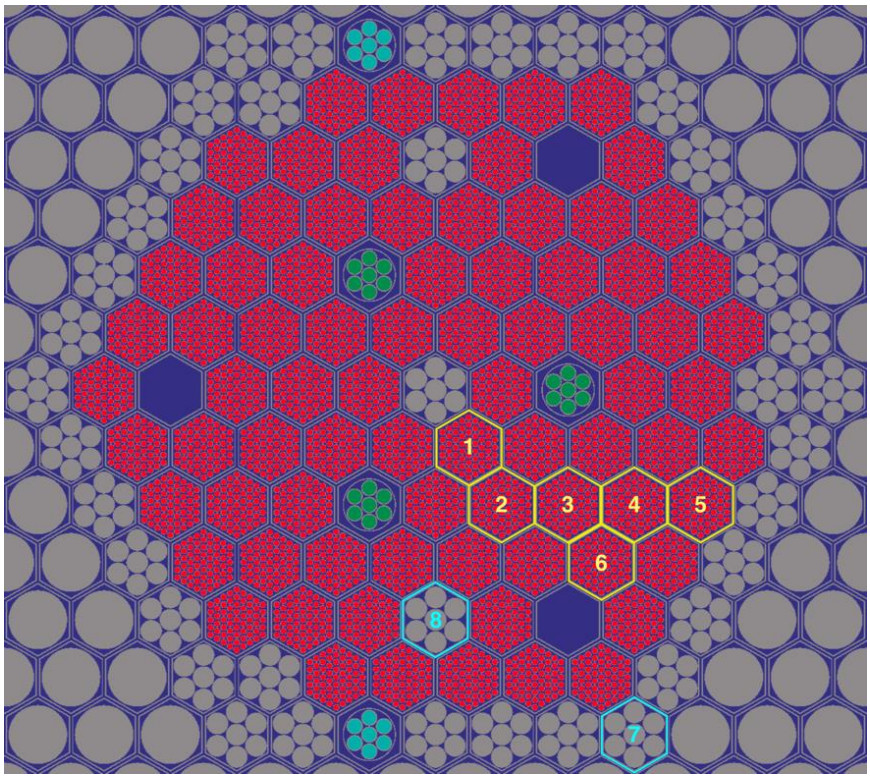

Figure 4.8 Locations for subassembly swap reactivity measurement

Table 4.10 Subassembly swap reactivity

Measurement position*		Temp (°C)	Evaluation		Measured	
			k-eff	Worth	Worth	error
#1 (2-6)	Original	250	0.99891	-885	-984	±13%
	Swapped	250	0.99016			
#2 (3-11)	Original	250	0.99891	-796	-875	
	Swapped	250	0.99103			
#3 (4-17)	Original	250	0.99891	-702	-772	
	Swapped	250	0.99195			
#4 (5-23)	Original	250	0.99891	-562	-639	
	Swapped	250	0.99333			
#5 (6-29)	Original	250	0.99891	-388	-476	
	Swapped	250	0.99505			
#6 (5-22)	Original	250	0.99891	-509	-586	
	Swapped	250	0.99386			
#7 (7-31)	Original	250	0.99505	175	210	
	Swapped	250	0.99679			
#8 (5-19)	Original	250	0.99881	555	582	
	Swapped	250	1.00438			

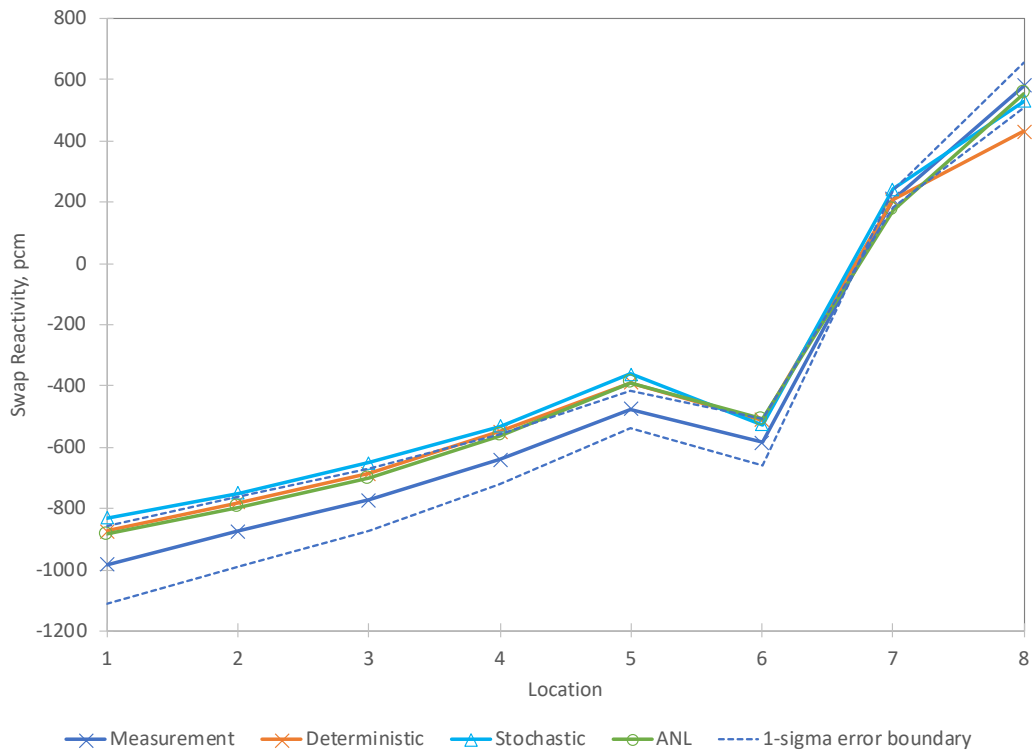

Figure 4.9 Comparison of swap reactivities

4.6 Foil reaction rate measurements

The foil activations were measured by enclosing foils in specially designed experimental subassemblies. Foils were loaded in eight radial positions for measurement of radial reaction distributions. The radial foil locations are shown in Figure 4.10. Position #1 is also used for the measurement of axial distribution, in which the irradiation foils were fixed at 14 axial positions. After irradiation in core, the activity was measured by high-purity- germanium spectrometer. Activation rates were measured for six reactions: U-235 (n,f), U-238 (n,f), Np-237 (n,f), Al-27 (n,α), Au-197 (n,γ), and Ni-58 (n,p). The measured reaction rates were normalized to the activation measured at the core center (for radial distribution) and the core mid-plane (for axial distribution). The measured radial and axial distributions of foil activation reactions are given in

Table 4.11 and Table 4.12, respectively.

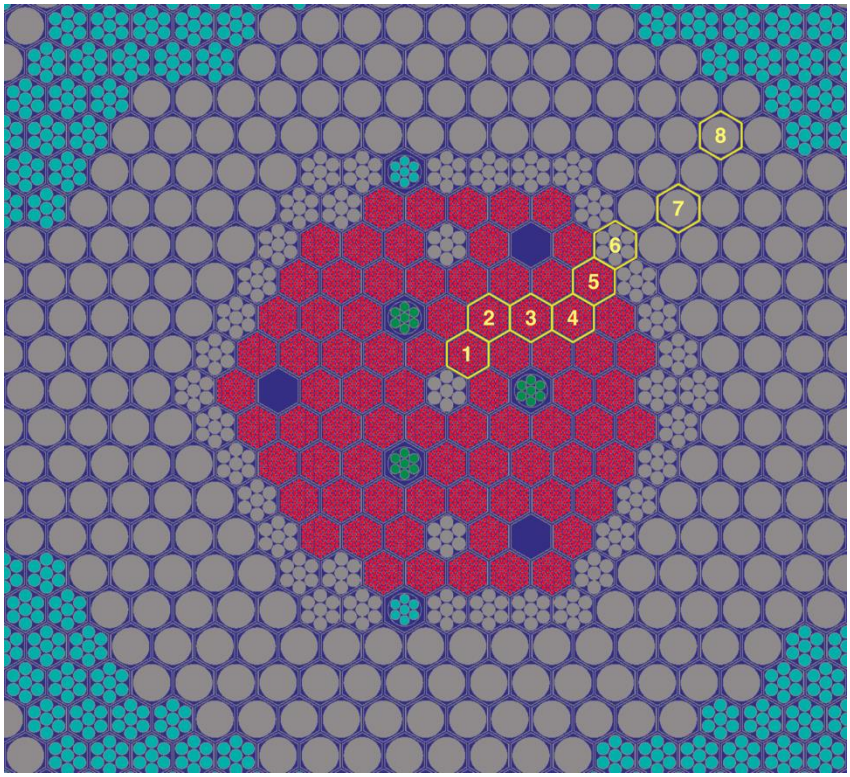

Figure 4.10 Radial locations for foil activation measurements

Table 4.11 Radial foil activation measurement

Radial Location	Control rod location, mm [a)]		U-235 (n,f)	U-238 (n,f)	Np-237 (n,f)	Au-197 (n,g)	Ni-58 (n,p)	Al-27 (n,a)
	RE1	RE2						
#1	241	241	1.00	1.00	1.00	1.00	1.00	1.00
#2	222	222	0.90	0.96	0.96	0.94	0.96	0.97
#3	198	199	0.84	0.92	0.91	0.93	0.94	0.91
#4	172	172	0.80	0.84	0.80	0.86	0.79	0.82
#5	147	149	0.65	0.61	0.58	1.00	0.59	0.58
#6	147	149	0.73	0.26	0.34	2.37	0.23	0.20
#7	147	149	0.72	0.05	0.09	4.01	0.03	0.03
#8	147	149	0.40	0.01	0.02	2.34	0.01	0.00

a) Shim rods are fixed at 247 mm

b) Coolant temperature in the experiment was 245 ^{o}C.

Table 4.12 Axial foul activation measurement

Axial location a)	U-235 (n,f)	U-238 (n,f)	Np-237 (n,f)	Au-197 (n,g)	Ni-58 (n,p)	Al-27 (n,a)
-425	0.52	0.05		1.72	0.04	0.04
-350	0.65	0.11	0.13	1.67	0.10	0.09
-250	0.79	0.37	0.43	1.35	0.36	0.33
-200	0.86	0.70	0.74	1.08	0.70	0.69
-150	0.94		0.88	1.01	0.89	
-100	0.99	0.94	0.96	1.01	0.98	0.95
-50	1.00	1.00	1.00	1.00	1.01	0.99
-25	0.98	0.98	0.98	0.99	1.00	1.00
0	0.97	0.95	0.96	0.96	0.98	0.96
50	0.92	0.92	0.87	0.90	0.90	0.90
100	0.79	0.79	0.73	0.81	0.78	0.81
200	0.60	0.44	0.38	0.88	0.33	0.41
250	0.49	0.22	0.21	1.08	0.16	0.18
300	0.42	0.12	0.11	1.32	0.08	0.09

a) RE1 and RE2 located at 247 mm and 246 mm, all shim rods located at 247 mm; coolant temperature in the experiment was 245 ^{o}C.

Figure 4.11 and Figure 4.12 show the measured radial and axial activation reaction distributions, respectively. Generally, except for the Au-197 (n,γ) reaction, the axial and radial activation reaction distributions have cosine shapes: i.e., the reactions are generally high at core center or midplane and low at core periphery and reflectors. However, the Au-197 (n,γ) reaction increases in radial reflector or axial blanket regions. The cross sections for the activation reactions of six isotopes are given in Appendix B. It is noted that Au-197 has a sizeable resonance capture cross section at 4.89 eV. Thus, the high Au-197 (n,γ) reaction rate at the radial reflector and axial blankets are high because of relatively higher epithermal neutrons in those regions.

The calculated radial and axial distributions of foil activation reaction rates are given in Table 4.13 and

Table 4.14, respectively. Except for Au-197 (n,γ) reaction rates, the calculated reaction rate distributions are well agreed with the measured reaction distributions. Radial and axial U-235 (n,f) reaction rate distributions are compared in Figure 4.13 and Figure 4.14, respectively, along

with results from several participants. The U-235 (n,f) rection rates are well predicted in driver and blanket regions, but it was slightly overestimated in the radial reflector regions.

Radial and axial Au-197 (n,γ) reaction rate distributions are compared in Figure 4.15 and Figure 4.16, respectively. Noticeable overestimations of the Au-197 (n,γ) reaction rate at radial reflector and axial blanket regions were observed. This trend is also observed in other participants. The primary reason of the overestimation is that the resonance self-shielding effect regarding the high capture cross section at 4.89 eV is not properly counted in the Au-197 (n,γ) reaction calculations. This effect is discussed in Section 6 in details.

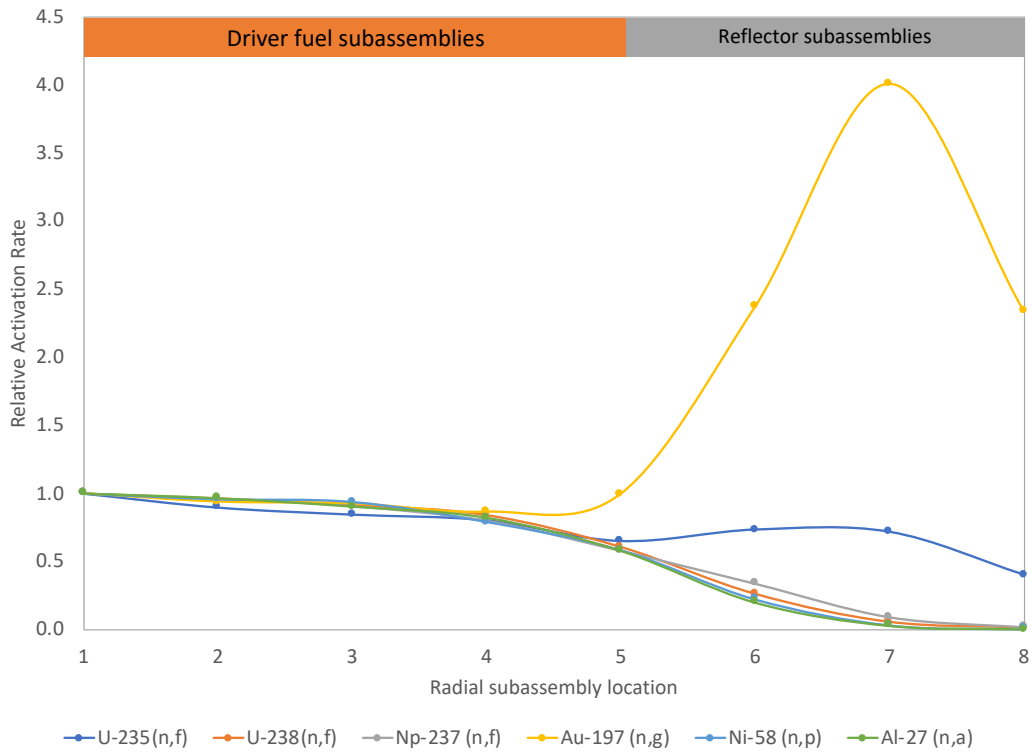

Figure 4.11 Radial distribution of measured foil activation

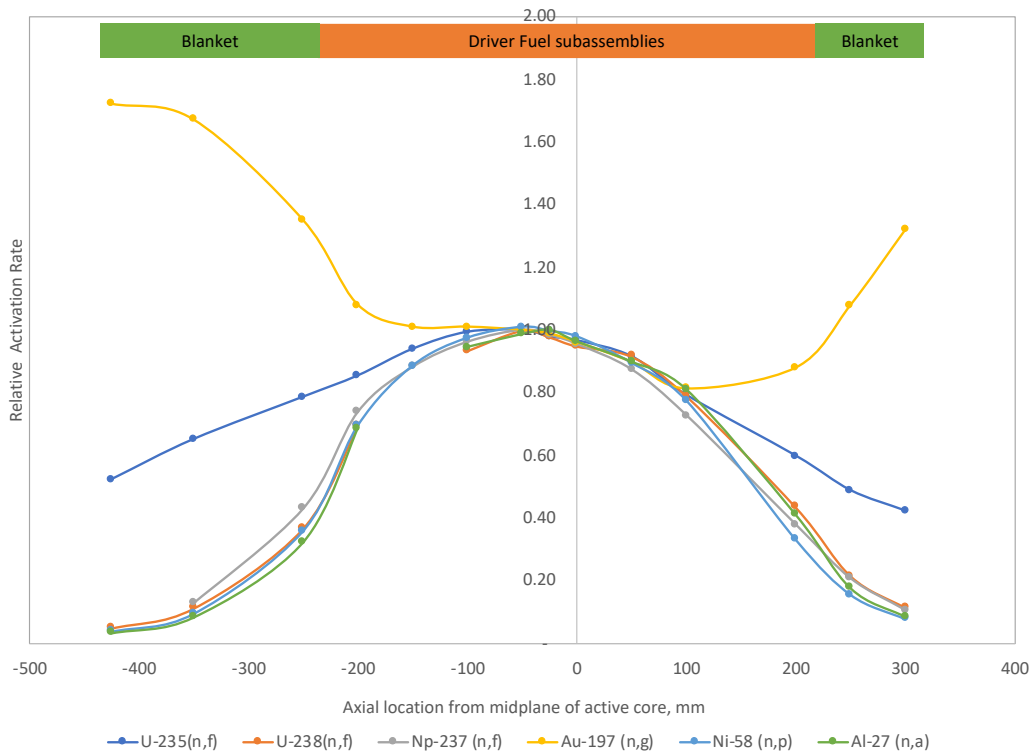

Figure 4.12 Axial distribution of measured foil activation

Table 4.13 Radial distribution of calculated activation foil reaction rates

Radial location	U-235 (n,f)	U-238 (n,f)	Np-237 (n,f)	Au-197 (n,g)	Ni-58 (n,p)	Al-27 (n,a)
#1	1.00	1.00	1.00	1.00	1.00	1.00
#2	0.95	0.98	0.97	0.94	1.00	1.01
#3	0.90	0.93	0.91	0.90	0.94	0.95
#4	0.82	0.83	0.81	0.89	0.84	0.85
#5	0.72	0.63	0.63	1.17	0.63	0.63
#6	0.86	0.26	0.34	5.01	0.22	0.19
#7	0.82	0.04	0.11	10.84	0.03	0.02
#8	0.44	0.01	0.03	6.46	0.00	0.00

Table 4.14 Axial distribution of calculated activation foil reaction rates

Distance from midplane, mm	U-238 (n,f)	Al-27 (n,a)	Distance from midplane, mm	U-235 (n,f)	Np-237 (n,f)	Au-197 (n,g)	Ni-58 (n,p)
324	0.093	0.071	340	0.41	0.119	2.259	0.078
271	0.191	0.161	286	0.49	0.207	1.497	0.156
220	0.441	0.427	233	0.58	0.384	1.040	0.348
118	0.812	0.811	131	0.79	0.782	0.802	0.780
66	0.918	0.916	77	0.90	0.901	0.885	0.899
14	0.982	0.980	25	0.97	0.974	0.957	0.973
-12	0.997	0.995	-3	0.99	0.994	0.984	0.993
-40	1.000	1.000	**-32**	1.00	1.000	1.000	1.000
-92	0.959	0.961	-84	0.98	0.966	1.003	0.966
-194	0.690	0.692	-138	0.92	0.875	0.973	0.878
-246	0.321	0.283	-190	0.83	0.711	1.005	0.705
-348	0.089	0.067	-244	0.76	0.400	1.735	0.342
-425	0.037	0.026	-347	0.64	0.140	2.517	0.091
			-425	0.53	0.066	3.247	0.036

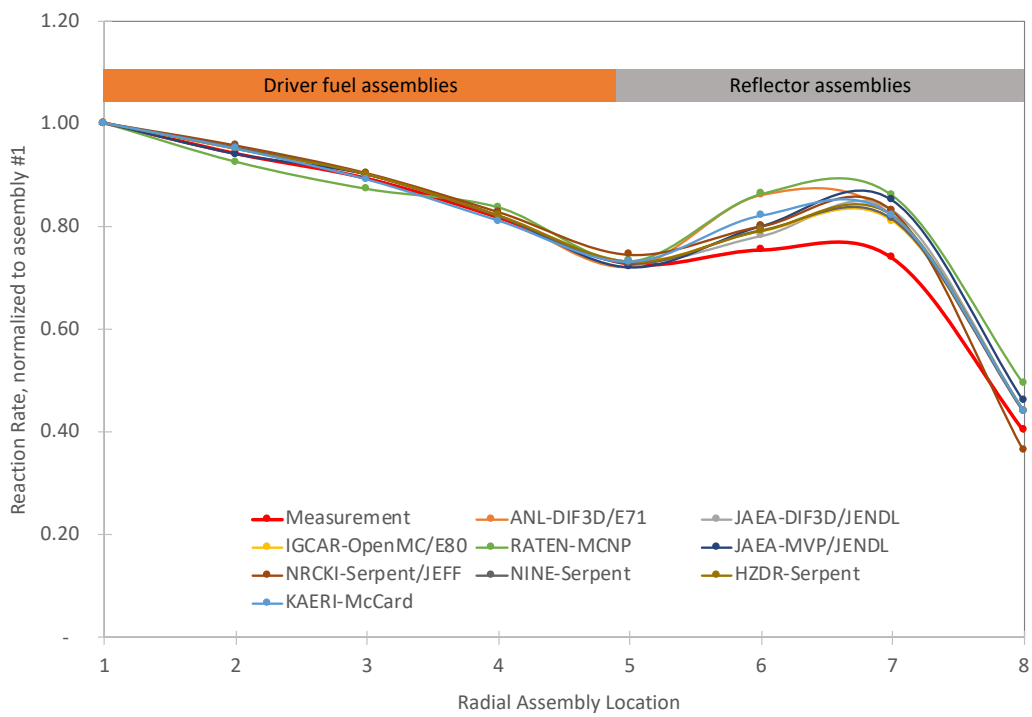

Figure 4.13 Comparison of radial U-235 (n,f) reaction rate distribution

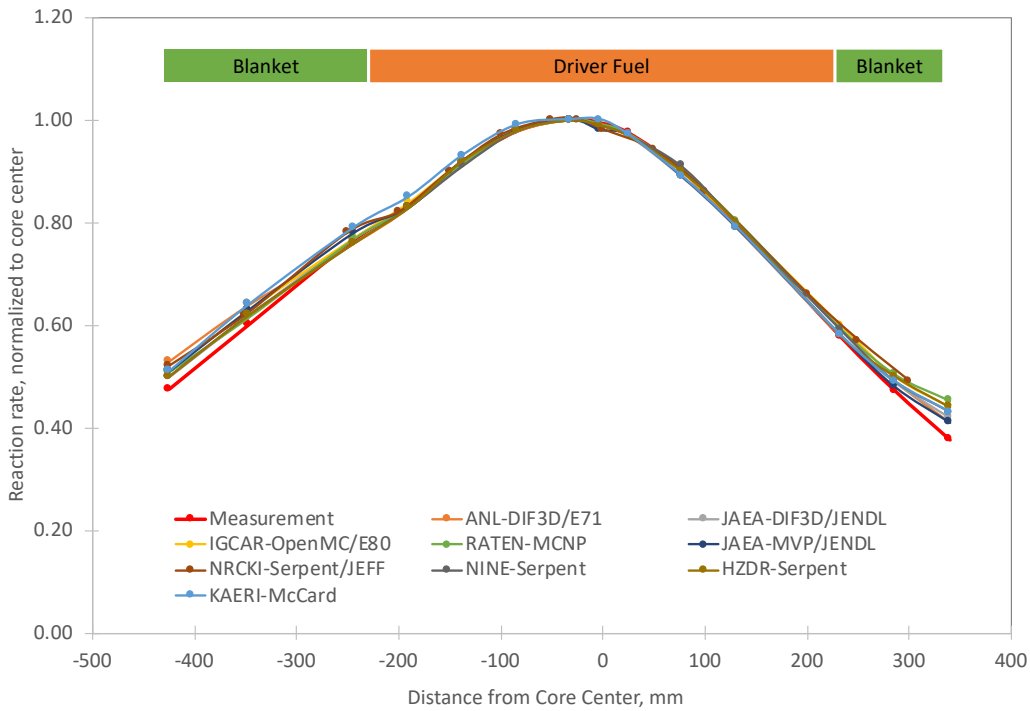

Figure 4.14 Comparison of axial U-235 (n,f) reaction rate distribution

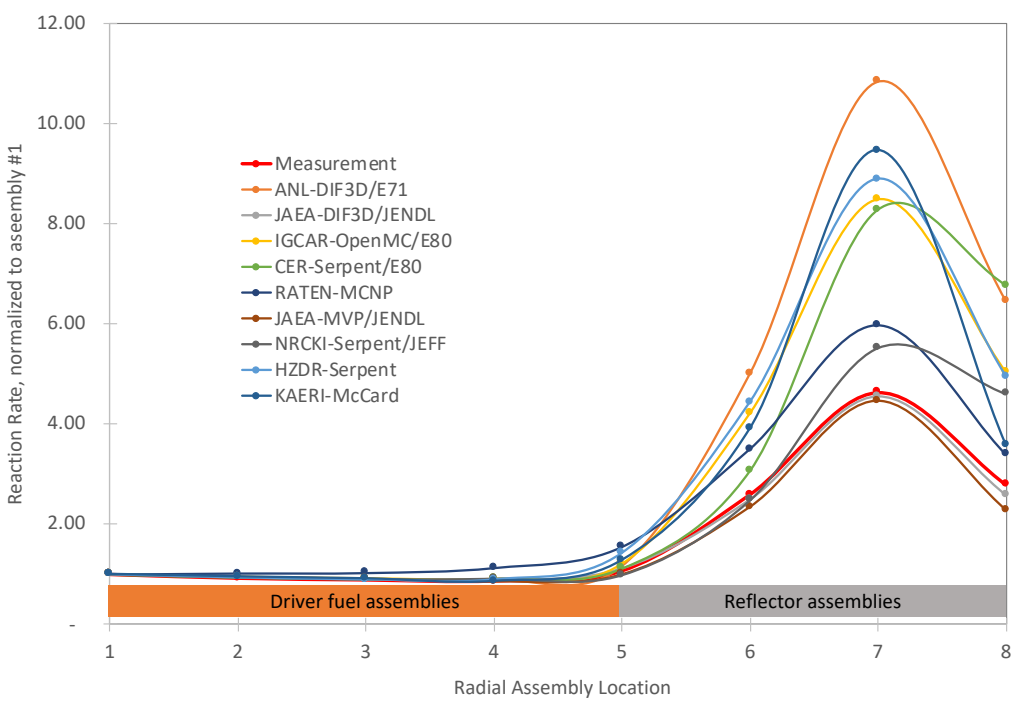

Figure 4.15 Comparison of radial Au-197 (n,γ) reaction rate distribution

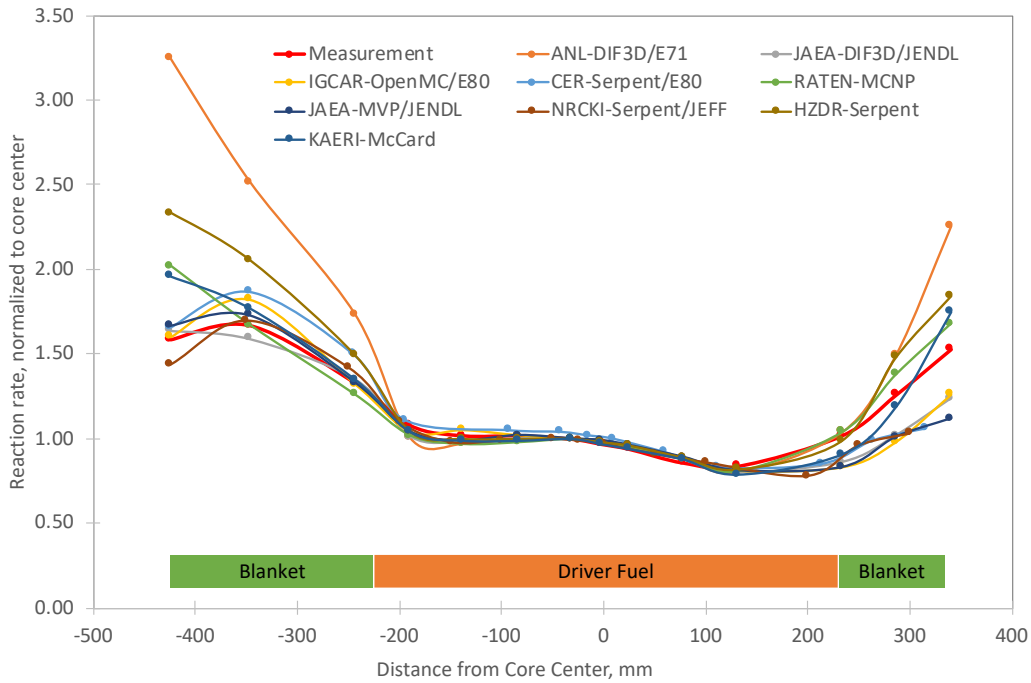

Figure 4.16 Comparison of axial Au-197 (n,γ) reaction rate distribution

5. Reactor Safety Parameters

In the kick-off meeting of the CRP in 2018 (Kriventsev et al. 2018), participants agreed to evaluate integral reactivity coefficients of the CEFR core. The integral reactivity coefficients include the Doppler coefficient, axial and radial thermal expansion coefficients, control rod expansion coefficient, and density coefficients of the fuel, coolant, and structural materials. Those coefficients have been defined by participants (Kim 2019) rather than measurement. Thus, the evaluation of integral reactivity coefficients is a purely numerical benchmark between participants.

5.1 Kinetics Parameters

The effective delayed neutron fraction, neutron generation time, and prompt neutron lifetime of the CEFR start-up core are calculated using the PERSENT code. The values are given in Table 5.1.

Table 5.1 Kinetics parameters for Operating Cold State (250˚C)

Group	β_{eff}
1	2.408E-04
2	1.252E-03
3	1.215E-03
4	2.764E-03
5	1.207E-03
6	5.057E-04
Total $\boldsymbol{\beta_{eff}}$	7.185E-03
Generation Time, nano-sec	278.9
Prompt Neutron Lifetime	278.6

5.2 Doppler coefficient and sodium void worth

Doppler constants at normal and flowing sodium voided states are defined by the core multiplication change from the normal state to fuel temperature perturbed states,

$$\Delta\rho_{normal}^{doppler}\left(\frac{pcm}{\Delta T}\right) = \frac{k_{normal}^{high\ temp.} - k^{normal}}{250\ K\ temperature\ change},$$

$$\Delta\rho_{voided}^{doppler}\left(\frac{pcm}{\Delta T}\right) = \frac{k_{voided}^{high\ temp.} - k_{voided}^{normal}}{250\ K\ temperature\ change},$$

where $k_{normal}^{high\ temp.}$, $k_{voided}^{high\ temp.}$, $k_{voided}^{normal.}$, and k^{normal} denote the core multiplication factors with high fuel temperature at the normal condition, high fuel temperature at the voided condition, normal operating temperature at voided condition, and the normal operation condition, respectively. For the fuel temperature perturbed case, the fuel temperature is increased to 500 ^{o}C from the normal operation fuel temperature of 250 ^{o}C. The sodium voided state is defined by the voided condition of flowing sodium inside duct of 79 fuel subassemblies from Lower

connector to handling head. Thus, the sodium in inter-fuel subassemblies (i.e., outside of duct of fuel assemblies) and the sodium in non-fuel subassemblies are not voided.

The Doppler constants calculated at the normal and sodium voided conditions are given in Table 5.2. Compared to Doppler constant at normal condition, Doppler constant at sodium voided condition is slightly less negative because of the reduced Doppler effect from hardened neutron spectrum. Doppler constants at normal and sodium voided conditions are compared with the results of participants in Figure 5.1 and Figure 5.2, respectively. For Doppler constant at normal condition, both deterministic and stochastic results are agreed well at in the range from -0.16 pcm/K to – 0.19 pcm/K, while Doppler constant at sodium voided condition has relatively large deviations.

Table 5.2 Doppler coefficient at normal and voided conditions

	Doppler Coefficient [pcm/K]
Normal Core	-0.18
Voided Core	-0.17

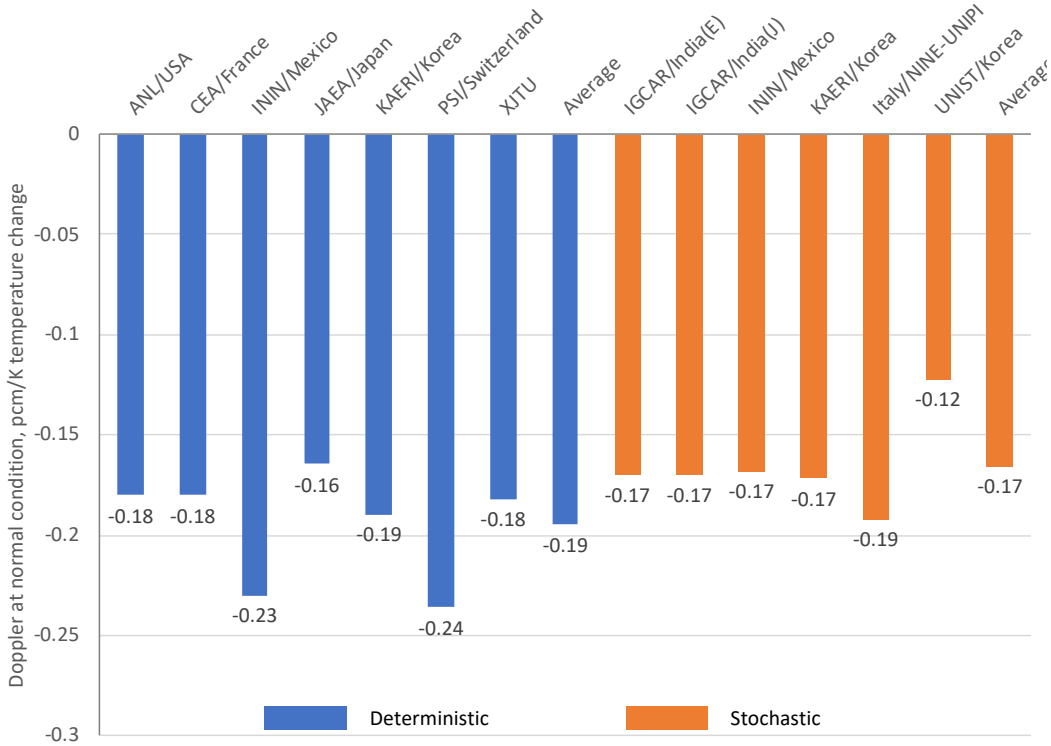

Figure 5.1 Comparison of Doppler constant at normal operation condition

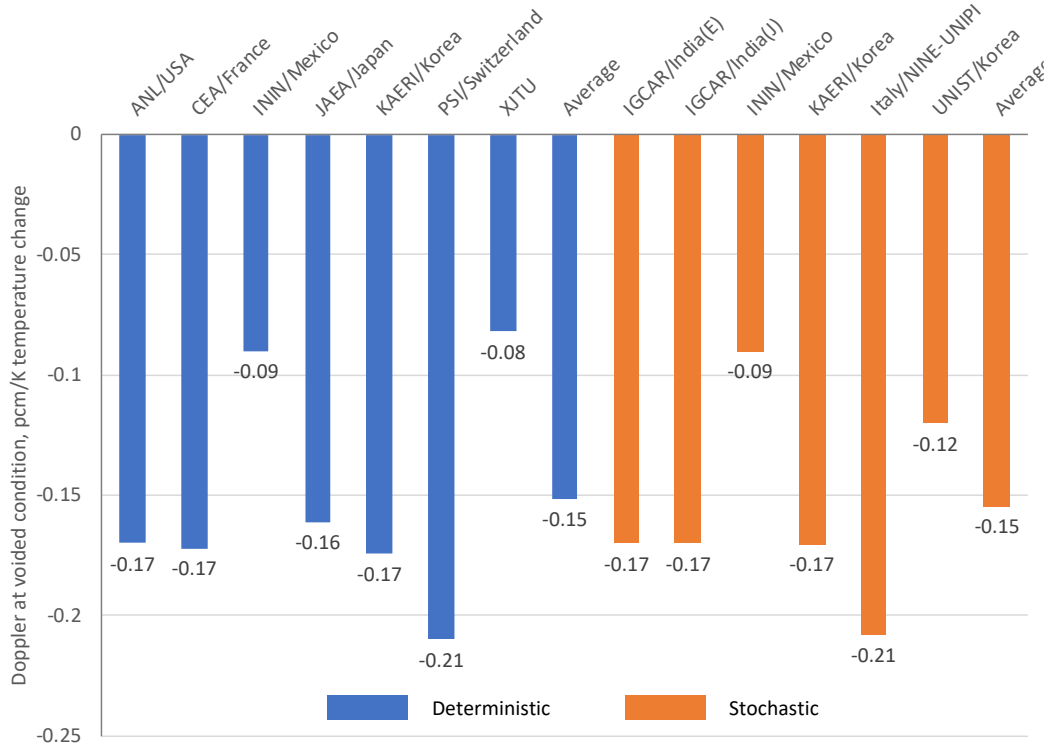

Figure 5.2 Comparison of Doppler constant at sodium voided condition

5.3 Axial and radial expansion coefficients

Axial and radial expansion reactivity coefficients are defined by the core multiplication change from the normal state to the 1% axially or radially expanded states,

$$\Delta\rho^{exp.}(\frac{pcm}{\%}) = \frac{k^{exp.} - k^{normal}}{1\%\ expansion},$$

where $k^{exp.}$ and k^{normal} denote the core multiplication factors at the expanded and normal states, respectively. Because fresh pellets are freely movable in cladding, it was assumed that only both fuel and blanket pellets are axially expanded by 1% and other structures (cladding, duct, etc.) are not axially expanded. For the radial expansion, it was assumed that the radial expansion is dictated by the grid plate and all subassemblies in the core are uniformly expanded radially by 1%. The driving force of the axial and radial expansions at the fresh fuel is thermal expansion per temperature change. For simplicity, however, participants agreed not to count the temperature change in the axial and radial expansion coefficient calculations. In addition, it was agreed that the control rods are in fixed positions, and the material densities are adjusted to conserve the original loading.

The CEFR core has negative thermal expansion coefficients. The calculated axial and radial expansion coefficients are -379 pcm/%-expansion and -885 pcm/%-expansion, respectively, and those are compared with the results of participants in Figure 5.3 and Figure 5.4. The most

probable axial and radial expansion coefficients are about -355 pcm/%-expansion and -885 pcm/%-expansion, respectively.

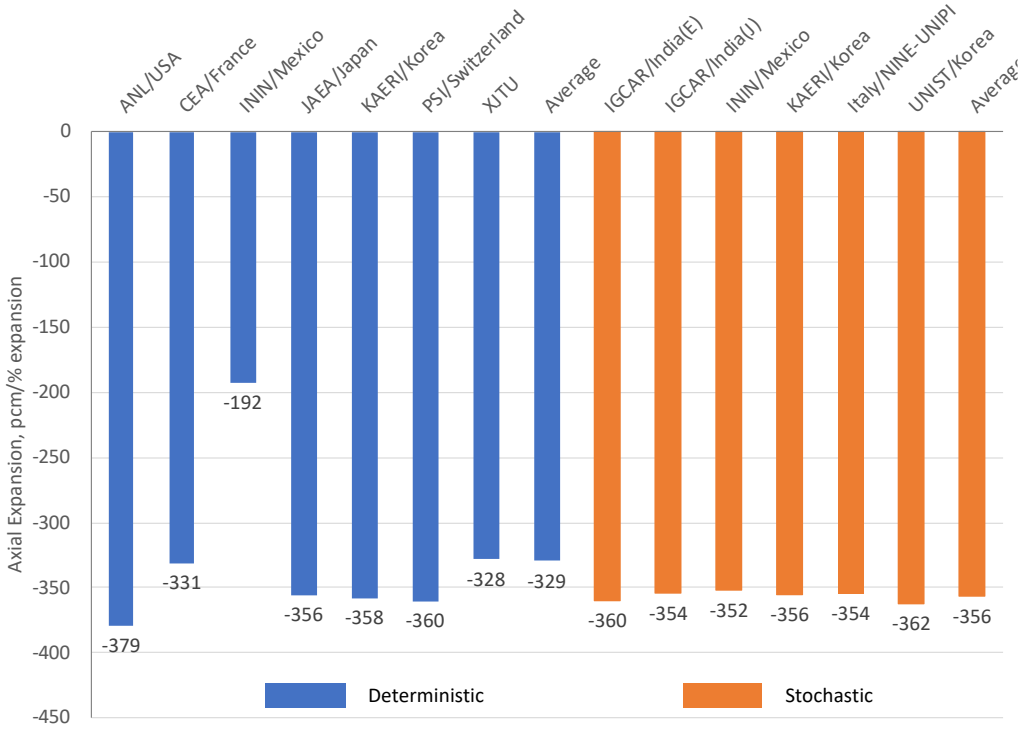

Figure 5.3 Comparison of axial expansion coefficients

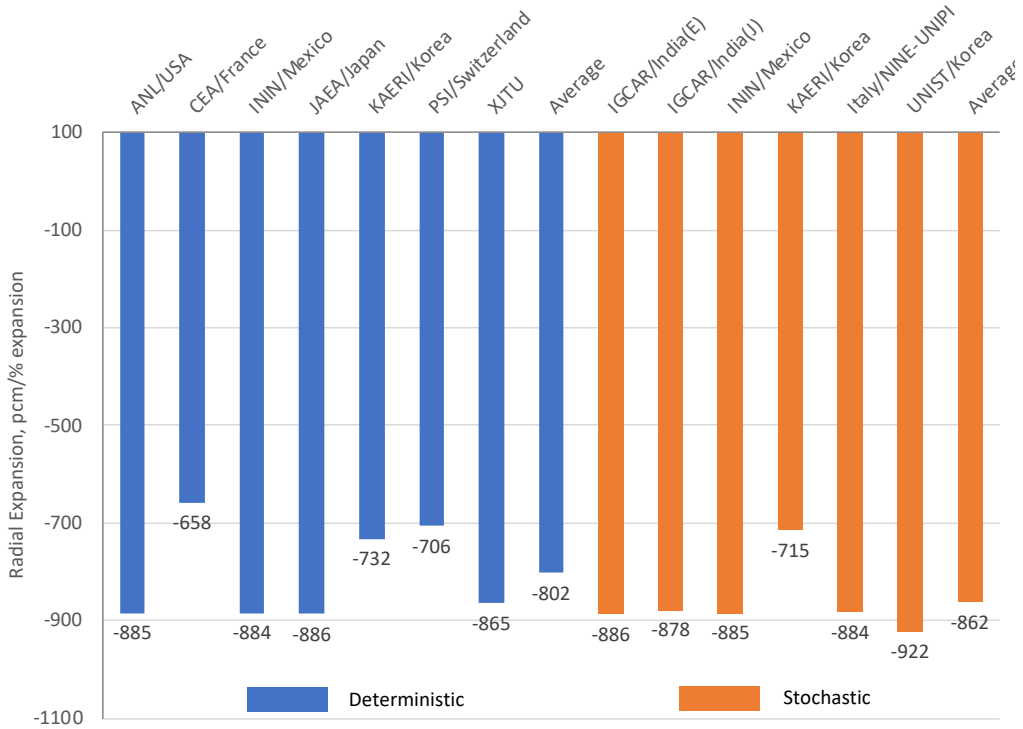

Figure 5.4 Comparison of radial expansion coefficients

5.4 Control rod expansion coefficients

Control rod expansion reactivity coefficient is defined by the core multiplication change from the normal state to the 10 cm control rod (CR) insertion by CR expansion,

$$\Delta\rho^{CR}_{regulating}\left(\frac{pcm}{cm}\right) = \frac{k^{CR\ insertion}_{regulating\ or\ shim} - k^{normal}}{10\ cm\ CR\ insertion},$$

where $k^{CR\ insertion}_{regulating,shim}$ is the core multiplication factor when regulating or shim CRs are inserted by 10 cm from the original critical positions.

The calculated regulating and shim control rod expansion coefficients are –8.8 pcm/cm and -156 pcm/cm, respectively. The shim control rod expansion coefficient is more negative than that of the regulating control rod because the shim rods locate at core central region with enriched boron and the regulating rods locate at core periphery with natural boron. The calculated regulating and shim control rod expansion coefficients are compared with the results of participants in Figure 5.5 and Figure 5.6, respectively. Generally, ANL values are more negative than the average values of participants. Stochastic codes estimated the regulating control rod expansion coefficients less negative than those calculated by deterministic codes. However, the shim control rod expansion coefficients are very consistent regardless of the computation methods.

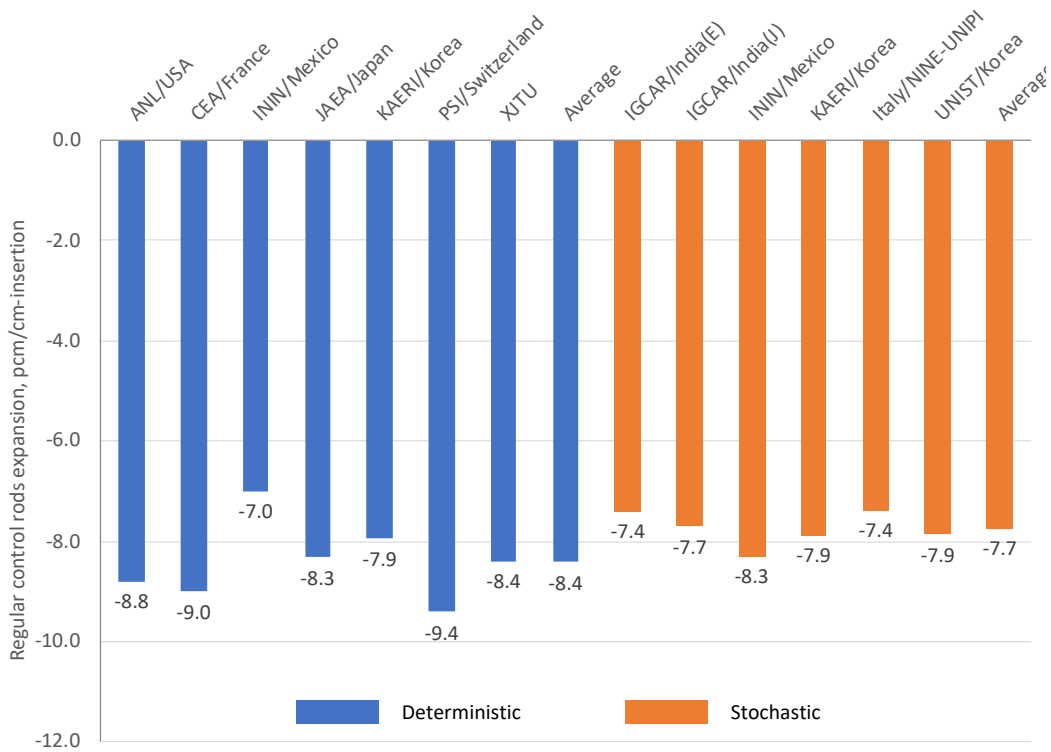

Figure 5.5 Comparison of regulating control rod expansion coefficients

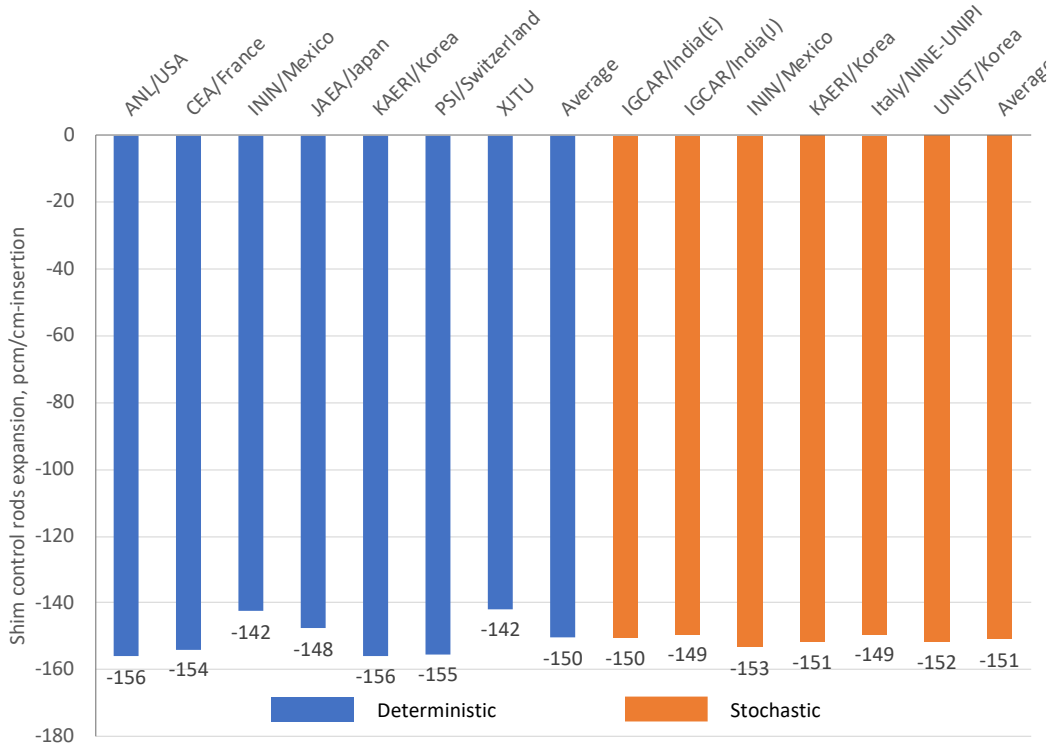

Figure 5.6 Comparison of shim control rod expansion coefficients

5.5 Density reactivity coefficients

Density reactivity coefficients of coolant sodium, steel, and fuel are defined by the core multiplication changes form the normal state to the density perturbed states;

$$\Delta\rho^{density}\left(\frac{pcm}{\%}\right) = \frac{k^{density} - k^{normal}}{1\%\ or\ 10\%\ density\ change},$$

where $k^{density}$ is the core multiplication factor of the density perturbed state. The density perturbed state is defined by 1% density increase in sodium and fuel (including upper blanket) pellet, but the steel density is increased by 10%. For simplicity, it was assumed that the density changes are only happened in 79 fuel subassemblies (i.e., densities of other subassemblies are not changed).

The calculated density coefficients for fuel, steel, and sodium 554.0 pcm/%-density-increase, 39.3 pcm/%-density-increase, and 31.4 pcm/%-density-increase, respectively. The density coefficients are compared with the results of participations in

The density reactivity coefficient of the fuel is approximately an order of magnitude greater than for the steel and sodium. The results are practically the same as with the blind phase model.

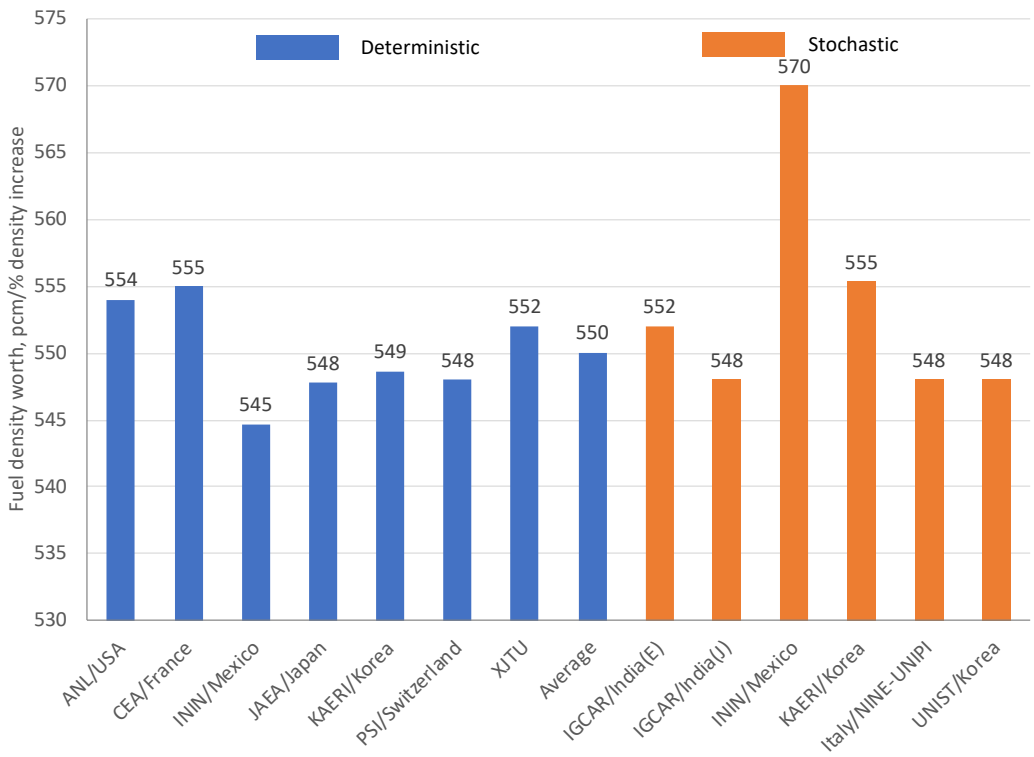

Figure 5.7 Comparison of fuel density coefficients

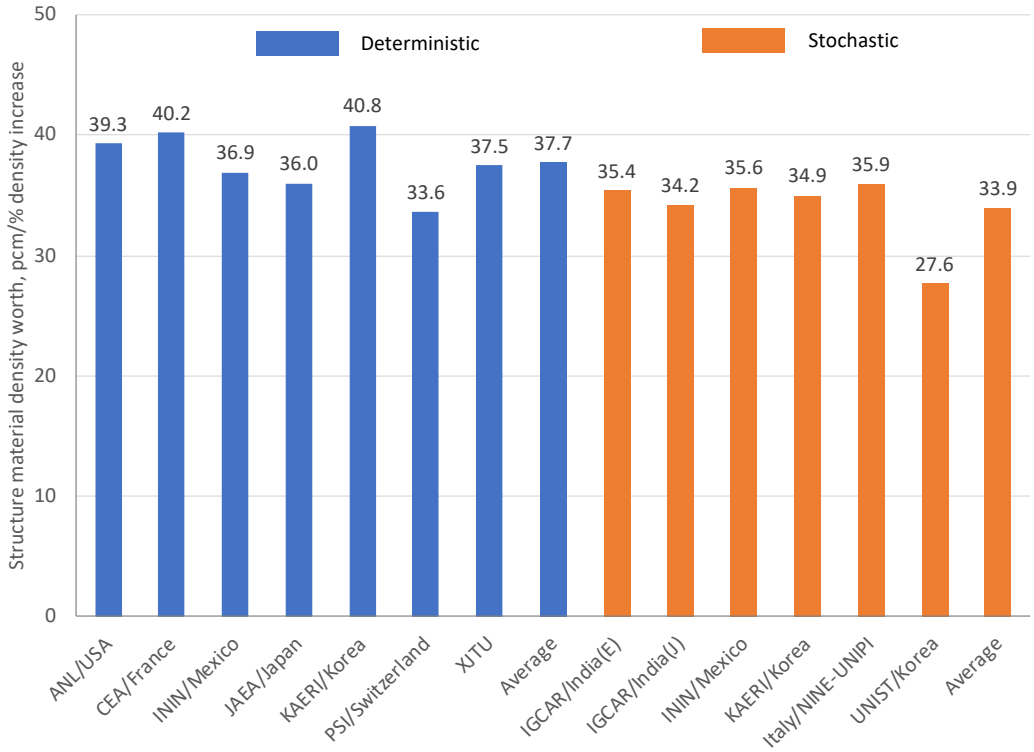

Figure 5.8 Comparison of steel density coefficients

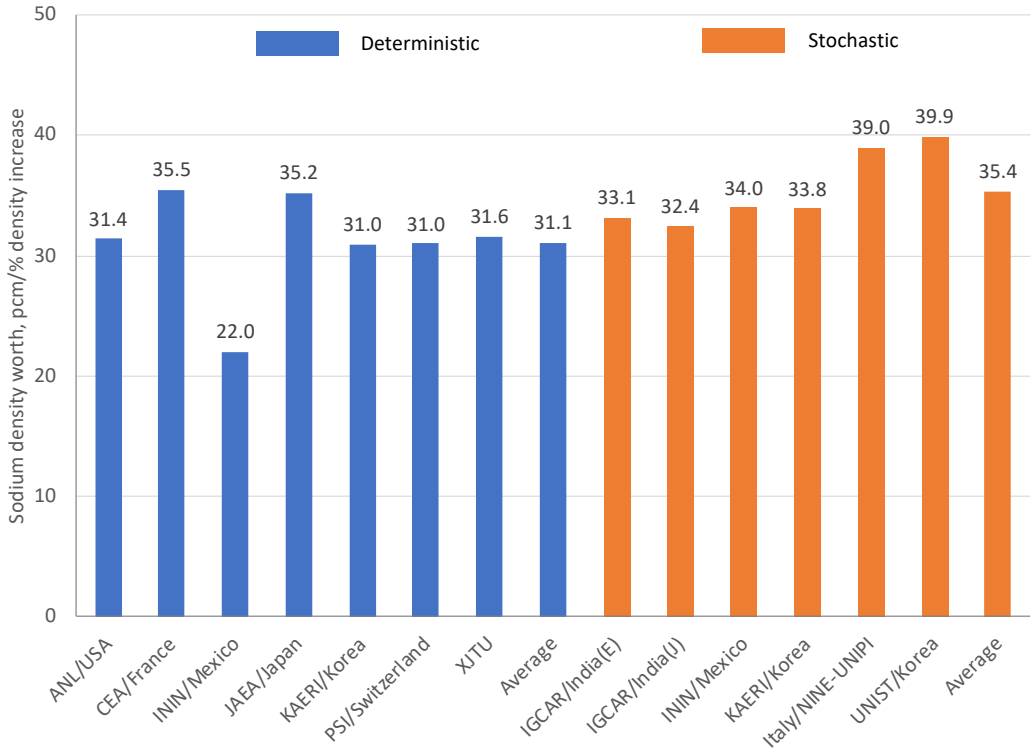

Figure 5.9 Comparison of sodium density coefficients

6. Further Investigation on Au-197 Foil Activation

Except for Au-197 foil activation measurements in radial reflector and axial blankets, the calculated parameters by the ARC code system are well agreed with the measured values in the CEFR start-up tests. For the Au-197 (n,γ) reaction distribution, a large discrepancy between the calculation and measurement values was observed in the radial reflector and blanket regions. A similar discrepancy was also observed by most participants regardless of deterministic and stochastic calculations. This informs that most participants have a common error in the calculation of the Au-197 (n,γ) reaction rate in radial and axial blankets. So, a further investigation has been carried out, and the new results are summarized in this section.

6.1 Investigation topics and computation models

Two further investigations have been conducted to resolve the large discrepancy between the calculations and measurement of the Au-197 (n,γ) reaction rate in the radial reflector and axial blankets, which are refinement of cross section group structure and correction of spatial self-shielding effect.

Refinement of cross section group structure

In the previous analyses, region-dependent 33-group cross sections were generated using the MC^2-3/TWODANT codes. Because the 33-group structure has been used for fast reactor design and analysis, there are only 3 groups below 5 eV. Generally, well-developed 33-group cross sections are sufficiently good to evaluate the major fast reactor design parameters, but it was observed in this CRP that the results using the 33-group cross sections produced a large error where a region contains high resonance nuclides in epithermal or thermal energy range. In the CEFR start-up test, Au-197 foils, which has a high resonance absorption at 4.89 eV, are distributed from the active core to the radial reflector and axial blankets where epithermal neutrons are dominant.

In the further investigation, the cross-section group structure was increased to 68 groups by adding more energy groups around the epithermal resonance of Au-197 at 4.89 eV. The comparison of the continuous energy and 68-group Au-197 (n,γ) cross sections is shown in Figure 6.1.

Correction of spatial self-shielding effect

The spatial self-shielding effect has not been considered in the previous calculations because the Au^{197} foil is very thin (0.03 mm), and most results from stochastic calculations are comparable to the results from deterministic calculations with a homogenous subassembly model. Most participants might not consider the spatial self-shielding effect as well because similar discrepancies are observed in the results of others (see Figure 4.15 and Figure 4.16). However, Clikeman et al. 1985 and Mo et al. 1987 claimed that the spatial self-shielding effect of high resonance isotopes could be substantial even though the foil is very thin. Thus, the spatial self-shielding effect of the Au-197 (n,γ) reaction at radial reflector and axial blankets was additionally evaluated in this work.

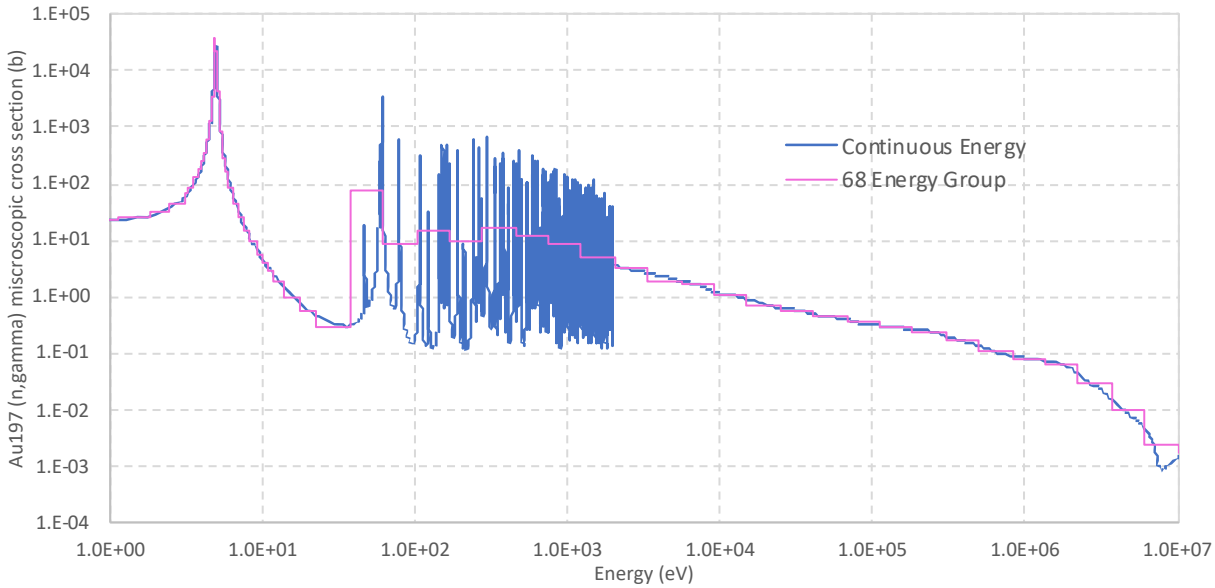

Figure 6.1 Comparison of the continuous energy and 68-group Au^{197} (n,γ) cross sections

To catch the spatial self-shielding effect, the 68-group cross sections at the experimental subassemblies (i.e., locations of foils) were regenerated by MC^2-3 using one-dimensional heterogeneous models shown in Figure 6.2. The foils are modeled inside the central experimental tube with the actual thickness.

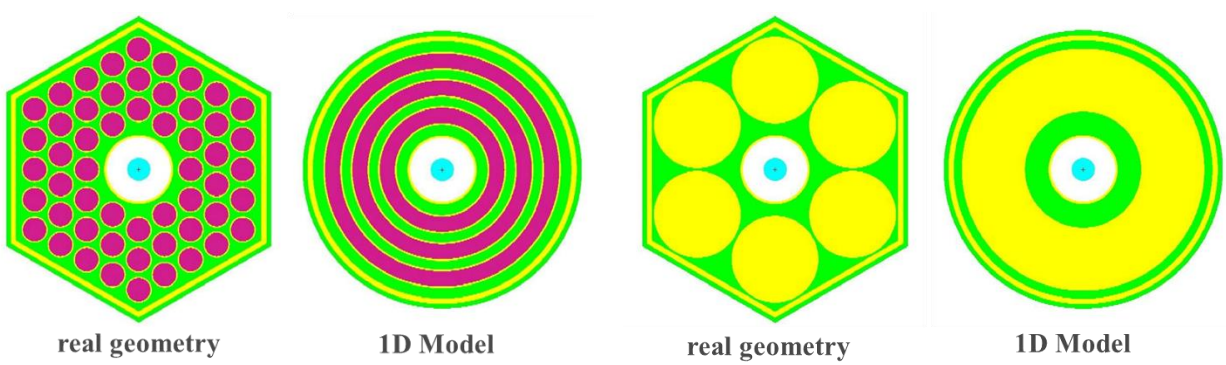

Experimental Fuel SA

Experimental Reflector SA

Figure 6.2 One-dimensional heterogeneous models of MC^2-3 for experimental SAs

6.2 Comparison of revised Au-197 (n,γ) reaction rate

Au-197 (n,γ) reaction rates were recalculated using the self-shielded 68-group cross sections, and the results were compared with the results obtained using the unself-shielded group cross sections. For a comparison purpose, the foil activation measurements were also calculated using

the MCNP6 code. In the MCNP6 calculations, foils were explicitly modeled ("shielded") and smeared into neighboring materials ("un-shielded"). All results are compared in **Error! Reference source not found.**Table 6.1, Table 6.2, Figure 6.3, and Figure 6.4.

Table 6.1 Axial reaction rate distribution of Au197(n,γ) reaction rate

Location (mm)	Measurement	Relative $Au^{197}(n,\gamma)$ reaction rate				
		DIF3D			MCNP6	
		33G, un-shielded	68G, un-shielded	68G, shielded	un-shielded	shielded
340	1.32	2.26	1.88	1.05	1.71(±3.73%)	1.16(±0.94%)
286	1.02	1.50	1.29	0.95	1.25(±2.86%)	0.98(±0.79%)
233	0.88	1.04	0.96	0.84	0.91(±2.70%)	0.84(±0.45%)
131	0.81	0.80	0.80	0.80	0.81(±0.22%)	0.81(±0.13%)
77	0.90	0.89	0.89	0.89	0.89(±0.15%)	0.89(±0.13%)
25	0.96	0.96	0.96	0.96	0.96(±0.16%)	0.96(±0.11%)
-3	0.99	0.98	0.98	0.98	0.98(±0.13%)	0.98(±0.11%)
-32	1.00	1.00	1.00	1.00	1.00(±0.16%)	1.00(±0.18%)
-84	1.01	1.00	1.00	1.00	1.00(±0.17%)	1.01(±0.12%)
-138	1.01	0.97	0.97	0.97	1.00(±0.33%)	1.00(±0.20%)
-190	1.08	1.01	1.00	0.99	1.04(±0.39%)	1.04(±0.26%)
-244	1.35	1.74	1.59	1.39	1.40(±0.82%)	1.33(±0.39%)
-347	1.67	2.52	1.89	1.61	1.82(±1.42%)	1.58(±0.53%)
-425		3.25				

Table 6.2 Radial reaction rate distribution of Au197(n,γ) reaction rate

Location	Measurement	Relative $Au^{197}(n,\gamma)$ reaction rate				
		DIF3D			MCNP6	
		33G, un-shielded	68G, un-shielded	68G, shielded	un-shielded	shielded
1	1.00	1.00	1.00	1.00	1.00(±0.13%)	1.00(±0.11%)
2	0.94	0.94	0.94	0.94	0.96(±1.19%)	0.94(±0.17%)
3	0.93	0.90	0.90	0.90	0.92(±0.96%)	0.91(±0.28%)
4	0.86	0.89	0.89	0.87	0.91(±1.36%)	0.89(±0.52%)
5	1.00	1.17	1.15	0.97	1.20(±1.66%)	1.05(±0.56%)
6	2.37	5.01	5.03	2.44	4.19(±2.32%)	2.39(±0.68%)
7	4.01	10.84	10.81	3.92	8.52(±1.84%)	4.06(±0.63%)
8	2.34	6.46	6.46	2.26	5.20(±2.55%)	2.36(±0.86%)

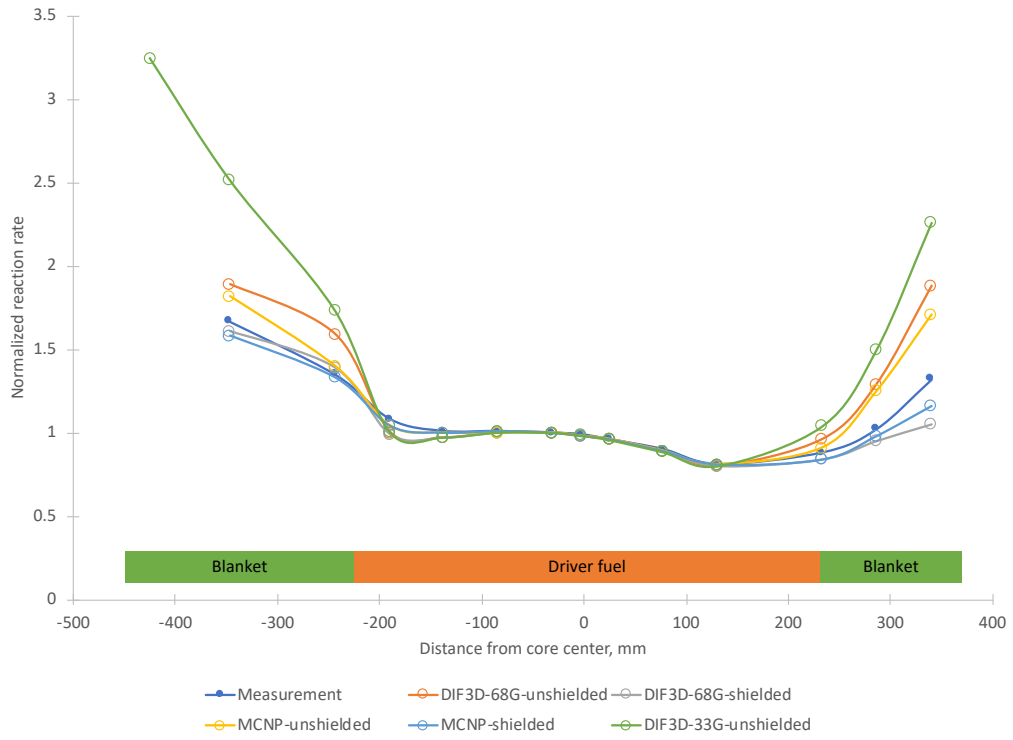

Figure 6.3 Axial profiles of $Au^{197}(n,\gamma)$ reaction rate

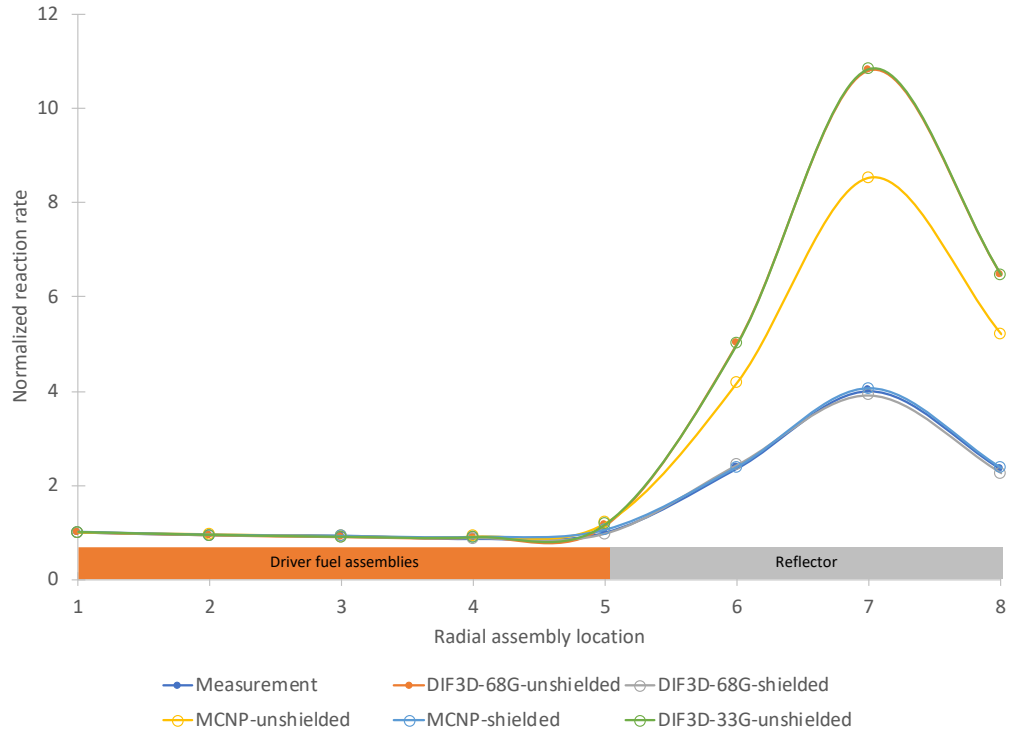

Figure 6.4 Radial profiles of $Au^{197}(n,\gamma)$ reaction rate

The MCNP6 results are generally comparable to the DIF3D results when the same self-shielding models are applied. This observation indicates that the computation methods (deterministic vs. stochastic) are not the cause of the large discrepancy of Au^{197} (n,γ).

When comparing the results obtained from the DIF3D calculations using unshielded cross sections, the axial Au^{197} (n,γ) reaction distribution using the 68-gorup cross sections was closer to the measurement compared to the results using the 33-group cross sections (see Figure 6.3). However, the Au^{197} (n,γ) reaction rates are still far different from the measurement in the radial reflector. Thus, this comparison indicates that the cross-section group structure is not the major reason of the large discrepancy. Additional detailed investigation on the cross-section group structure is summarized in Appendix C.

However, the DIF3D results are agreed well with the measurements when using the “shielded” cross sections. Similar agreement was observed in the MCNP6 calculations when the self-shielding effect was well modeled. Thus, it could be concluded that the primary reason of the large discrepancy of Au-197 (n,γ) reaction rates between the calculations and measurements in the radial reflector and axial blanket was due to the poor modeling of spatial self-shielding effect. In the driver fuel region, fast neutrons dominate and as a result, the spatial self-shielding effect of Au-197 was small. However, in the reflector region, the neutron spectrum is much softer than the fuel region and the spatial self-shielding effect becomes significant.

This further investigation gave an important lesson on the fast reactor analysis. Reactor designer or analyst should review the reactor-specific physics and material characteristics before the modeling of the core. Otherwise, calculated reactor physics parameters may contain large errors as observed in the Au-197 (n,γ) activation measurement.

7. Conclusions and Observations

The Chinese Experimental Fast Reactor (CEFR), a 65MWt Sodium-cooled Fast Reactor with highly enriched uranium-oxide (UO_2) fuel, achieved the first criticality in 2010, followed by a start-up test to measure reactor physics parameters that are needed for reactor operation safely. In 2018, the International Atomic Energy Agency (IAEA) launched a Coordinated Research Project (CRP) on "*Neutronics Benchmark of CEFR Start-Up Tests*" to utilize the start-up test data for validation and qualification of member states computation capabilities. Twenty-nine international organizations from eighteen member countries, including Argonne National Laboratory, committed to participate in the CRP.

The benchmark consists of six experimental measurements, including criticality per fuel loading, control rod worth, sodium void reactivity, temperature reactivity coefficient, subassembly swap reactivity, and foil activations. Participants also agreed on the numerical benchmark to evaluate integral reactivity coefficients for understanding the integral safety feature of the CEFR core, even though those have not been measured in the start-up tests. The integral reactivity coefficients are Doppler constant, density reactivity coefficient, kinetics parameters, sodium void reactivity coefficients, and thermal expansion coefficients. CIAE provided the benchmark specifications, including the CEFR design data, drawings, start-up test conditions, measured data, and experimental uncertainties.

The CRP has been conducted through two phases: blind and open phases. In the blind benchmark, each participant calculated the parameters measured in the start-up test using the given benchmark specifications, but without measured data. In the following open benchmark, participants could access the measured data and the results from other participants. The blind phase was completed in 2019, and results from the open benchmark were shared with other participants in April 2021.

All benchmark calculations were conducted using the Argonne Reactor Computation (ARC) code suite. The region-dependent multi-group cross sections were generated using the MC^2-3/TWODANT code, and the whole core transport calculations were performed by the DIF3D-VARIANT code. Except for the Au-197 (n,γ) reaction rate in the radial reflector and axial blankets, the results are generally well agreed with the measurements. For instance, the calculated core multiplication factor for the given CEFR critical configuration is 0.99890, which is 110 pcm lower than the criticality. Other parameters, such as control rod worth, sodium void worth, temperature reactivity coefficient, subassembly swap reactivity, and foil activation rates, are agreed with the measured values within the one standard deviation of the experimental uncertainties.

A noticeable discrepancy between calculation and measurement was observed in the Au-197 (n,γ) reaction rates in the radial reflector and axial blankets. The primary reason for the discrepancy was poor modeling of the spatial self-shielding effect of the Au-197 (n,γ) reaction in the epithermal energy range. Through further investigation, it was observed that the large discrepancy was poor modeling of the spatial self-shielding effect of Au-197 (n,γ) reaction rate in the regions where the epithermal neutrons are dominant. Au-197 has a high resonance capture

at 4.89 eV, and the spatial self-shielding effect is significant even though the foil is very thin. In addition, a relatively coarse group structure of 33-group cross sections in the epithermal energy region was a reason (but minor) for the discrepancy. In this work, the discrepancy was resolved by modeling the spatial self-shielding effect in the cross-section generation and increasing the cross-section groups to 68 groups. The new calculations using the self-shielded and refined group structure cross sections gave good agreements of Au-197 (n,γ) reaction rates with the measurement in the radial reflector and axial blankets.

The CRP was a good opportunity to validate the ARC code suite by comparing the results with the measured data and the results calculated by various participants with both deterministic and stochastic reactor analysis codes. Additionally, the followings are observed in the CRP:

- Except for several outliers, the accuracies of both deterministic calculations and stochastic calculations are comparable to each other (see the comparison of criticality and sodium void worth in Figure 4.2 and Figure 4.6, respectively). Note that the outliers are mainly due to the misunderstanding of the experiments or inaccurate cross sections,
- The results could be different even though the same reactor analysis codes were used. For instance, several participants used the DIF3D and Serpent codes for deterministic and stochastic calculations, respectively. However, as shown in Figure 4.2, the results are different depending on the neutron libraries, cross sections generation methods, and modeling of the core. This observation informs that experiences of fast reactor analyses and knowledge on computation codes are important factors to have accurate results.
- Reactor-specific physics and material characteristics should be well captured in the modeling and simulation. Otherwise, calculated reactor physics parameters may contain large errors as observed in the Au-197 (n,γ) activation measurement (see section 4.6 and section 6).

References

Alcouffe, R., F. Brinkley, D. Marr and R. O'dell (1994), "User's Guide for TWODANT: A Code Package for Two-Dimensional, Diffusion-Accelerated Neutral Particle Transport," Los Alamos National Laboratory, 1984.

Clikeman, F. M., S. C. Mo, and K.O. Ott, “Neutron Reaction Rate Measurements as Tests of Diffusion Calculations in a Fast Breeder Blanket Facility,” Nuclear Technology, 71(1), pp. 341-352 (1985).

Huo, X. (2018), "Technical Specification for Neutronics Benchmark of CEFR Start-up Tests (CRP-I31032) - Draft," KY-IAEA-CEFRCRP-001, China Institute of Atomic Energy, Dec. 2019.

Huo, X. (2019), "Technical Specification for Neutronics Benchmark of CEFR Start-up Tests (CRP-I31032),Version 7.0," KY-IAEA-CEFRCRP-001, China Institute of Atomic Energy, May 2018.

IAEA (2018), “Neutronics Benchmark of CEFR Start-up Tests,” International Atomic Energy Agency, https://www.iaea.org/projects/crp/i31032 (2018).

Jarrett, M. and T. Kim (2019), "Evaluation of China Experimental Fast Reactor Startup Tests," ANL/NSE-19/27, Argonne National Laboratory, September 2019.

Kim, T. K. (2019), “Appendix A. Benchmark Specifications of Integral Reactivity Coefficients,” International Atomic Energy Agency, 2018.

Kriventsev V., et al., (2018) “IAEA CRPs on Fast Reactors and Introduction of New CRP on Neutronics Benchmark of CEFR Start-up Tests,” First RCM of IAEA CRP, June 11-14, Vienna (2018)

Lee, C., and N. Stauff (2015), "Improved Reactivity Estimation of MC^2-3/DIF3D for Fast Reactor Analysis," in Trans. Am. Nucl. Society, San Antonio, TX, April 19023, 2015.

Mo, S. C., and K. O. Ott (1987), “Resonance Self-Shielding Corrections for Detector Foils in Fast Neutron Spectra”, Nucl. Sci. Eng., 95(3), pp. 214-224 (1987).

APPENDIX A. LIST OF PATICIPANTS

Table A. 1 List of participants using deterministic codes

Country	Institute	Evaluated nuclear data	multigroup cross section code	Core analysis code
Belgium	SCK.CEN	ENDF/B-VII.1		OpenMC
China	CIAE	ENDF/B-VIII	PASC, HADC	NAS
	FDS			SuperMC
	INEST			
	XJTU	ENDF/B-VII	SARAX-TULIP	SARAX-LAVENDER
Finland	VTT	ENDF/B-VII, JEFF-3.1		Serpent 2.1.31
France	CEA	JEFF 3.1	ECOO	VARIANT/SNATCH
Germany	HZDR	JEFF-3.1, 3.3, ENDF/B-VII.1, VIII.0		Serpent 2.1.31
	KIT	JEFF 3.1	ECCO	VARIANT
	GRS	ENDF/B-VII	Serpent 2	FENNECS
Hungary	CER	ENDF/B-VIII	Serpent	KIKO3DMG
India	IGCAR	FOND-2 (ABBN-93) JEFF2.2 (ERALIB1) ENDF/B-VIII.0	CONSYST+COHINT ECOO	FARCOB+DORT HEX3D + BISTRO OpenMC
Italy	NINE-UNIPI	ENDF/B-VIII		Serpent 2.1.31, MCNP
Japan	JAEA	JENDL 4.0	SLAROM-UF	DIF3D/PARTISN MVP-II
Korea	KAERI	ENDF/B-VII	MC^2-3	DIF3D/VARIANT McCard 1.0
	UNIST	ENDF/B-VII.1	MCS	MCS RAST-K
Mexico	ININ	ENDF/B-VIII	Serpent 2	AZNHEX 3.0
Romania	RATEN	ENDF/B-VIII.0		MCNP6.1, Serpent 2
Russia	IPPE	ROSFOND10+		MMKC
	Kurchatov	FOND-2 (ABBN-93)	CONSYST	JARFR
	SSL	ENDF/B-VII	WIMS4D	DYNCO
Slovakia	VUJE	ENDF/B-VII.1		Serpent 2.1.31
Switzerland	PSI	JEFF 3.1.1	Serpent 2	PARCS
Ukraine	KIPT	(BNAB-78)		FABTEBS-2D
UK	Univ. Cambridge	JEFF 3.1.2	WIMS 11	WIMS 11
USA	ANL/US	ENDF-B/VII	MC^2-3	DIF3D/VARIANT
	NRC	ENDF-B/VII		Serpent 2.1.30

APPENDIX B. FOIL ISOTOPE CROSS SECTIONS

Al-27 (3.2 MeV) and Ni-58 (800 keV) are both threshold reactions; the cross section is not significant for either below several MeV. Al-27 and Ni-58 ENDF/B-VIII.0 cross sections are given in Figure B.1 and Figure B.2.

The radiative capture cross section for Au-197 is given in Figure B.3. The Au-197 (n,γ) reaction peaks in the reflector region because the cross section is higher for thermal neutrons. The calculated reaction rate for Au-197 is much higher than the measured rate; the size of the 4.89 eV capture resonance for Au-197 may be impacting the flux spectrum and straining the infinite dilution approximation used in MC^2-3 and DIF3D-VARIANT.

The (n,f) cross sections for U-235, U238, and Np-237 are given in Figure B.4, Figure B.5 and Figure B.6. U-238 has a negligible (n,f) cross section below 1 MeV. Np-237 has a relatively low fission cross section below 1 MeV, but it is not as low as U-238. U-235 has a much larger thermal and epithermal neutron cross section.

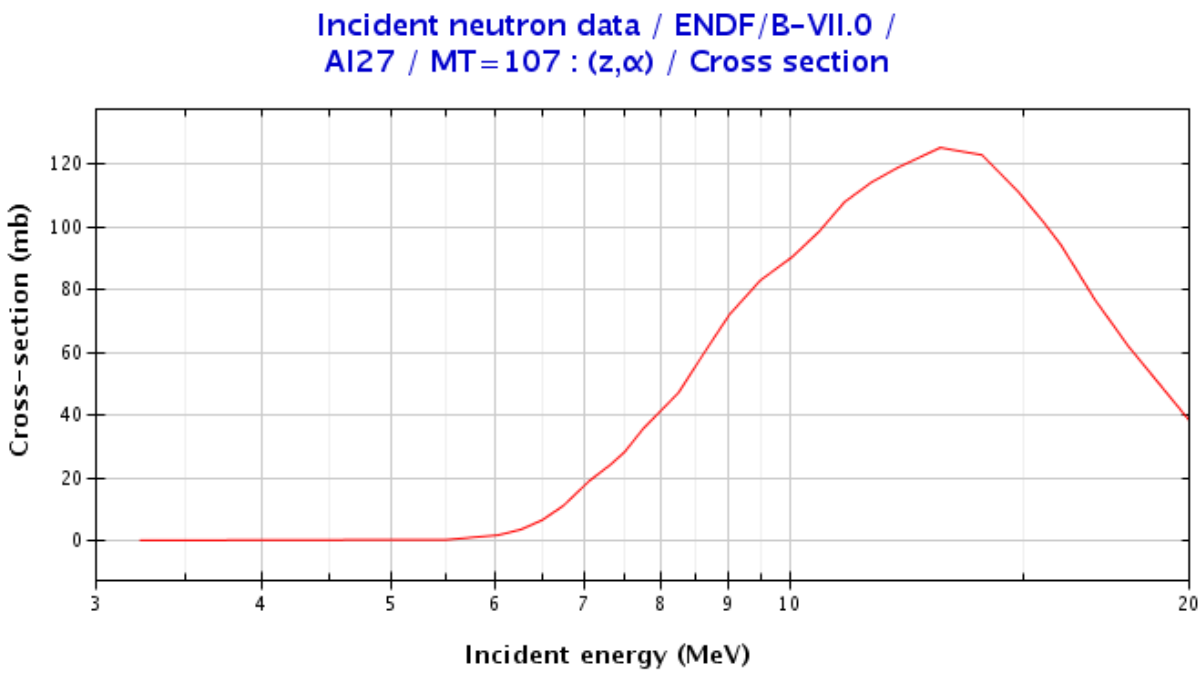

Figure B.1 Al-27 (n,α) ENDF/B-VIII.0 cross section data

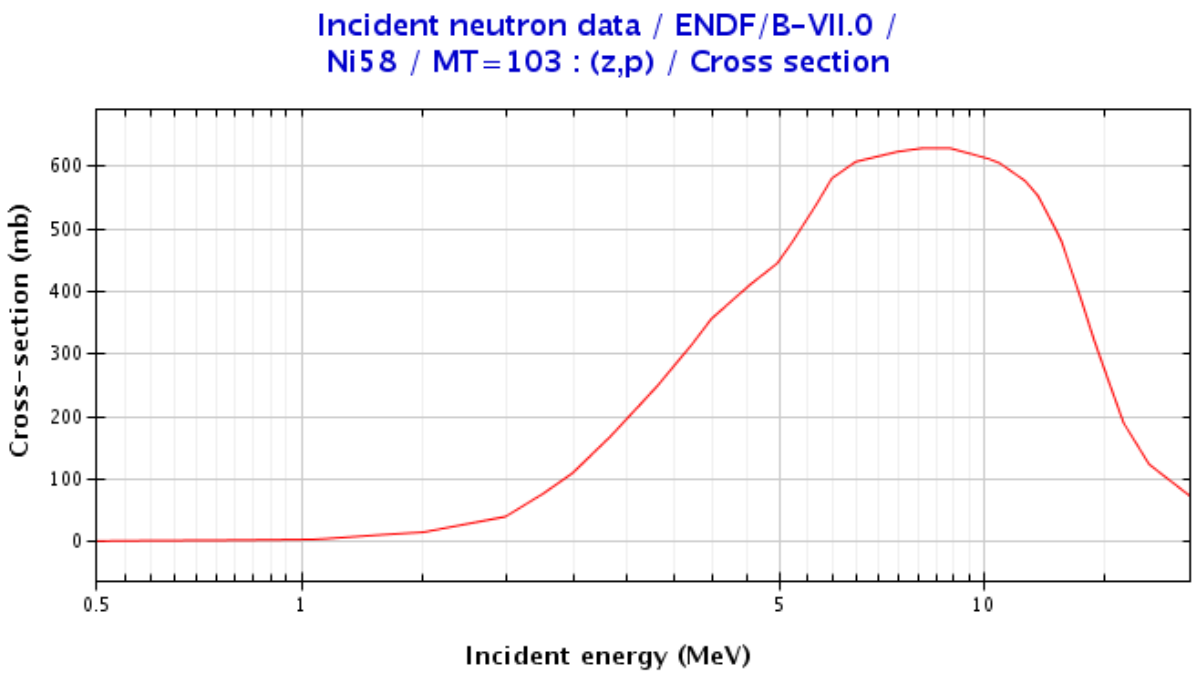

Figure B.2 Ni-58 (n,p) cross section ENDF/B-VIII.0 cross section data

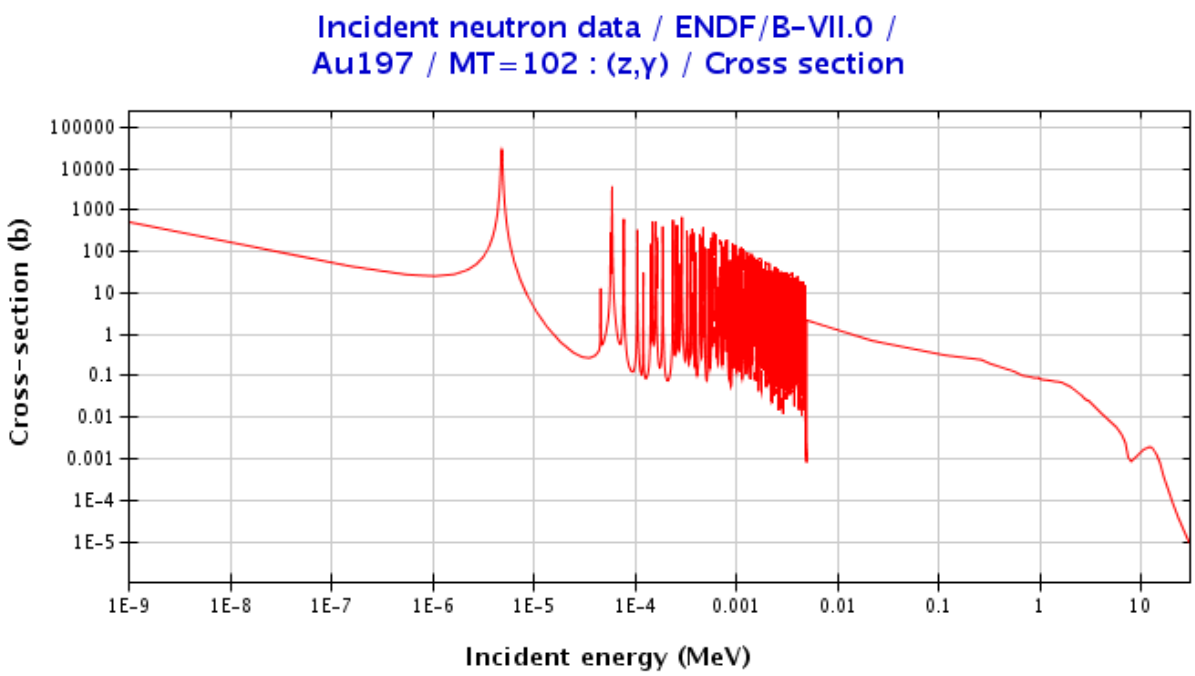

Figure B.3 Au-197 (n,γ) ENDF/B-VIII.0 cross section data

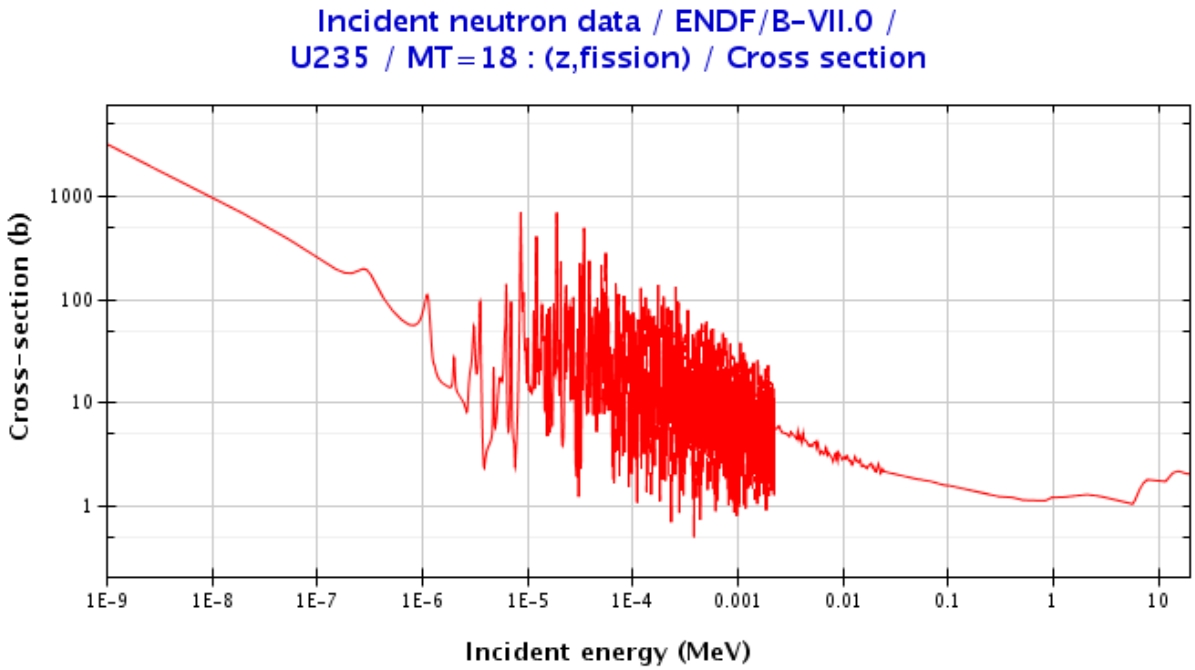

Figure B.4 U-235 (n,f) ENDF/B-VIII.0 cross section data

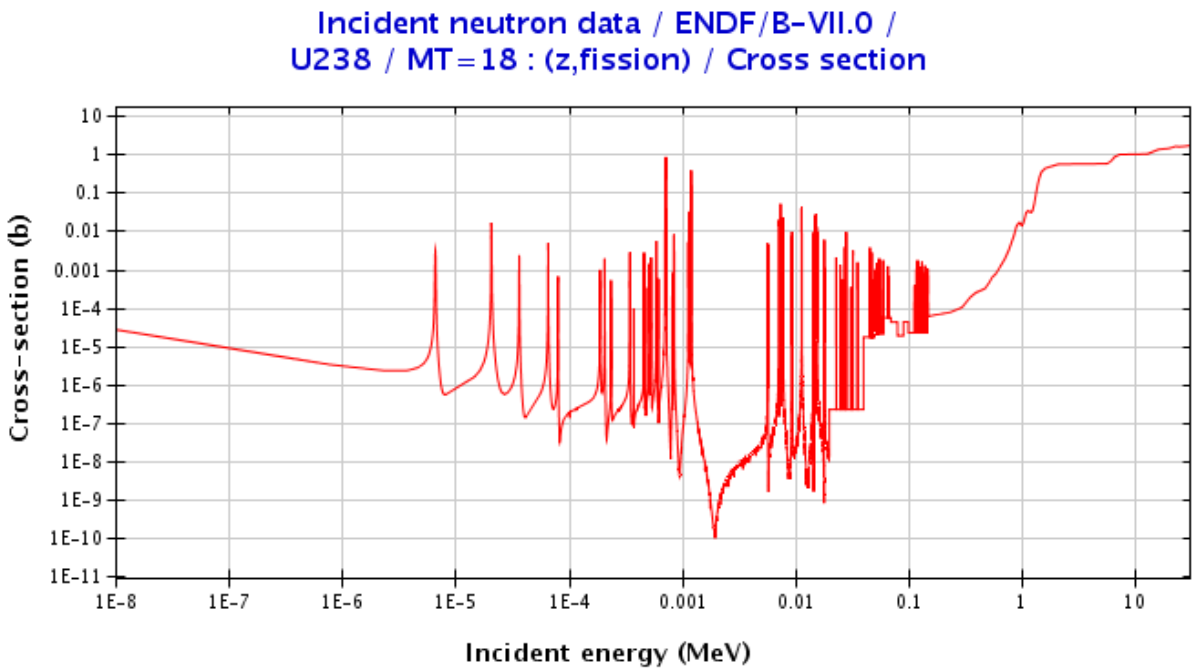

Figure B.5 U-238 (n,f) ENDF/B-VIII.0 cross section data

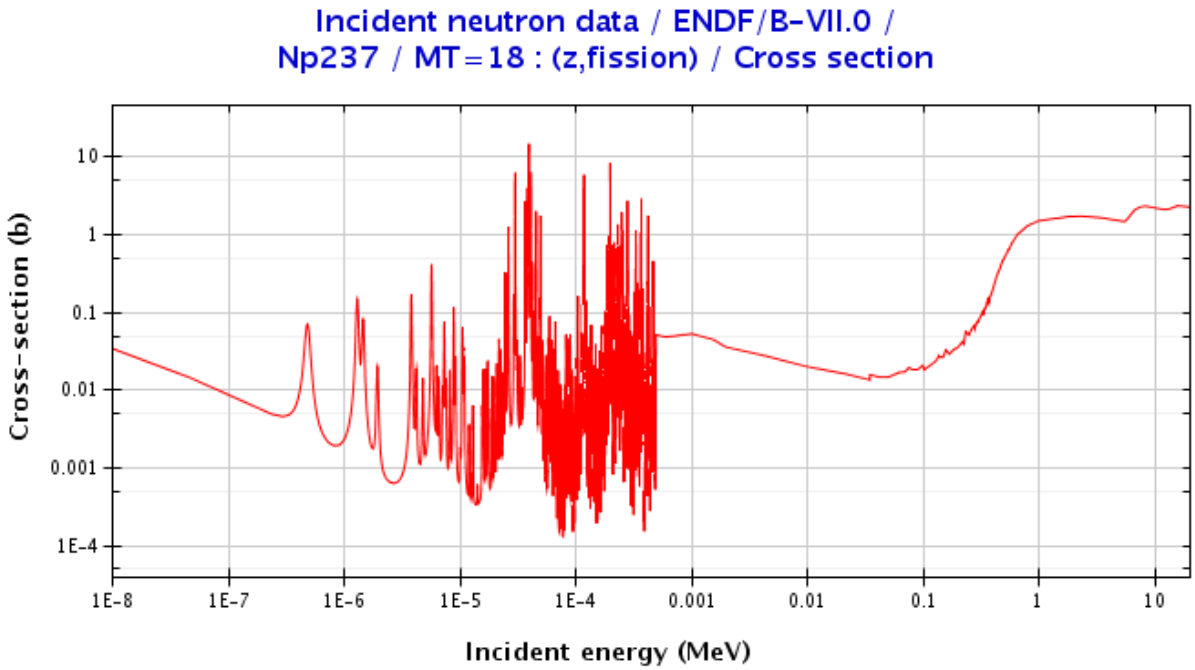

Figure B.6 Np-237 (n,f) ENDF/B-VIII.0 cross section data

APPENDIX C. INVESTIGATION ON CROSS-SECTION GROUP STRUCTURE

The calculated reaction rate distributions from DIF3D-VARIANT for interactions attributable mostly or entirely to fast neutrons were generally in good agreement with the measured values. These reactions include U-238 and Np-237 fission, Ni-58 (n,p) and Al-27 (n,α). However, the accuracy was much worse for interactions dominated by epithermal and lower-energy neutrons, especially far from the active core. U-235 fission and even Au-197 capture reaction are dominated by fast neutrons in the active core, but epithermal/low-energy (~5 eV, still above thermal) neutrons become an increasingly significant contributor at distances farther from the active core, as the fast flux decays and the epithermal flux grows. The Au-197 neutron capture interaction has very large cross sections at lower energies, including the resonance of 27,000 barn at 4.89 eV.

The relative contribution of each energy range to the total reaction rate at each of the eight radial locations is shown in Table B.1. Inside the active core (locations 1-5), the unresolved resonance (above 2 keV) and fast neutron spectrum dominates the Au-197 (n,γ) reaction. Outside of the active core, the resolved resonances become more important, especially the region below approximately 40 eV, where most of the reactions are produced by the wide resonance centered at 4.89 eV. The 4.89 eV resonance is mostly contained within group 31 of 33 in the multigroup structure.

Table C.1 Relative Au-197 (n,γ) reaction rate contribution per different energy regimes

Assembly Location	4.89 eV Resonance	Other Resolved Resonance	Unresolved Resonance and Fast Spectrum
1	0.1%	5.9%	94.0%
2	0.2%	5.5%	94.3%
3	0.5%	6.1%	93.4%
4	3.6%	9.1%	87.3%
5	21.7%	18.8%	59.5%
6	62.6%	24.3%	13.1%
7	75.7%	20.2%	4.2%
8	77.3%	19.2%	3.5%

The fluxes, cross sections, and reaction rates in radial location 7 (in the radial reflector region) are shown in Figure B.1. Since the whole resonance is contained within a single group, we might expect a relatively large error associated with the multigroup approximation here. This is observed in the large over-estimation of reaction rate for this isotope in the ex-core regions. The Au-197 is effectively infinitely diluted in the material in MC^2-3 for generating the cross section. This dilution should be a reasonable approximation because the mass of the foil is small compared to the other materials but given the very high resonance peak for this reaction it may be a source of error. The foil itself is not modeled in DIF3D-VARIANT.

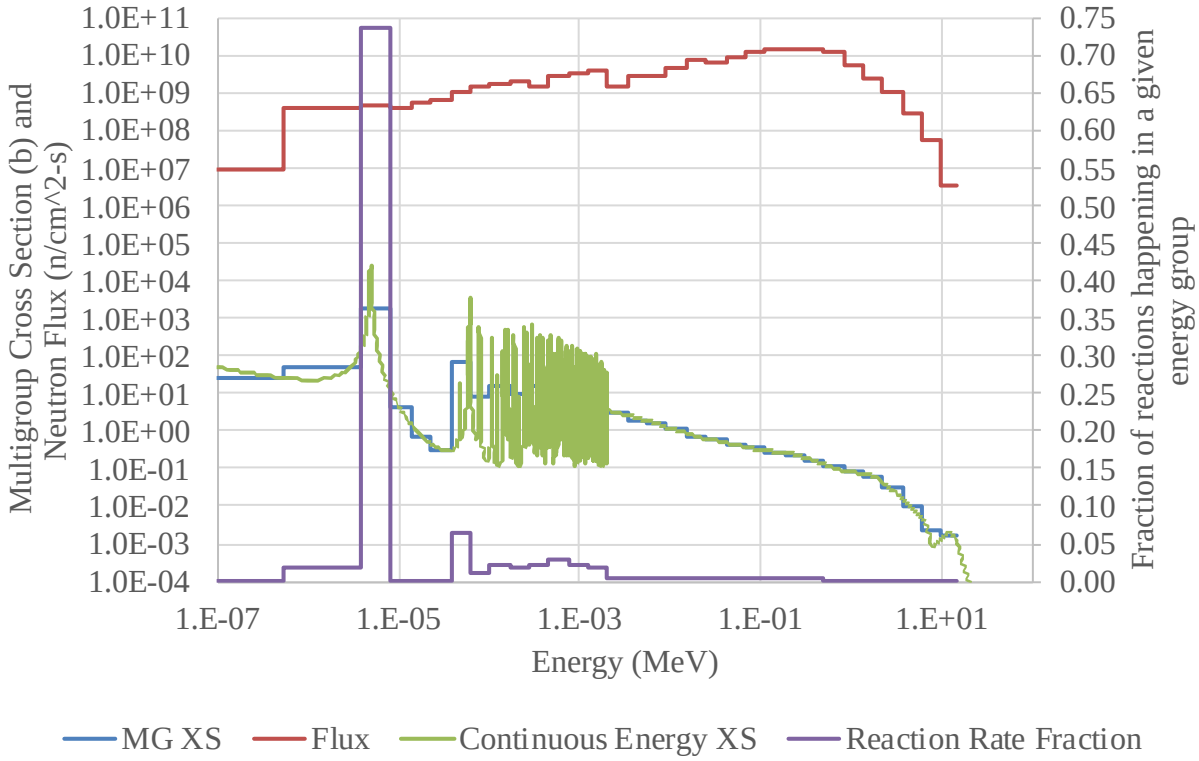

Figure C.1 Flux, cross section, and Au-197 (n,γ) reaction rate in radial reflector

The typical 33-group structure used in DIF3D-VARIANT is not designed to accurately capture the neutron energy spectrum at low energies because these neutrons do not typically contribute significantly to quantities of interest for fast reactor operation. However, the comparison to measured reaction rates, especially for Au-197 capture, shows that DIF3D-VARIANT with 33 groups has a significant error for low-energy neutrons outside of the core. The finer broad-group structures available in MC^2-3 (70, 116, or 230 groups) are not typically used because the memory requirements and run time quickly grow with the increasing number of energy groups. When the low-energy neutron spectrum is important, it may be worthwhile to use more groups to limit the error associated with the multigroup approximation.

To determine whether increasing the number of groups improves the result, the radial distributions of Au-197 (n,γ) reactions calculated with 33 groups and 70 groups are compared in Table B.2. The axial distributions are compared in Table B.3. The 70-group library does not significantly improve the calculated radial reaction rate. This suggests that the source of the error may be in the infinite dilution approximation, and not in the multigroup structure itself. The flux and reaction rates with 70 groups are compared in Figure B.2. The wide 4.89 eV resonance is represented by five groups in the 33-group structure, and 20 groups in the 70-group structure, but the vast majority of the reactions associated with the resonance still

happen within a single energy group in the 70-group structure. Thus, the finer energy group structure does not do much to improve the energy resolution of the resonance peak.

Table C.2 Radial distribution of Au-197 neutron capture reaction rate

Measurement Position*	Relative Au-197 (n,γ) reaction rate		
	70 groups	33 groups	Measured
#1 (2-2)	1.00	1.00	1.00
#2 (3-3)	0.94	0.94	0.94
#3 (4-3)	0.90	0.90	0.93
#4 (5-3)	0.90	0.89	0.86
#5 (6-4)	1.16	1.17	1.00
#6 (7-5)	4.97	5.01	2.37
#7 (9-6)	10.61	10.84	4.01
#8 (11-8)	6.36	6.46	2.34

Table C.3 Axial distribution of Au-197 neutron capture reaction rate

Distance from midplane (mm)	Relative Au-197 (n,γ) reaction rate		
	70 groups	33 groups	Measured
340	2.10	2.26	1.32
286	1.40	1.50	1.02
233	1.00	1.04	0.88
131	0.80	0.80	0.81
77	0.88	0.89	0.90
25	0.96	0.96	0.96
-3	0.98	0.98	0.99
-32	1.00	1.00	1.00
-84	1.00	1.00	1.01
-138	0.98	0.97	1.01
-190	1.00	1.01	1.08
-244	1.63	1.73	1.35
-347	2.22	2.52	1.67

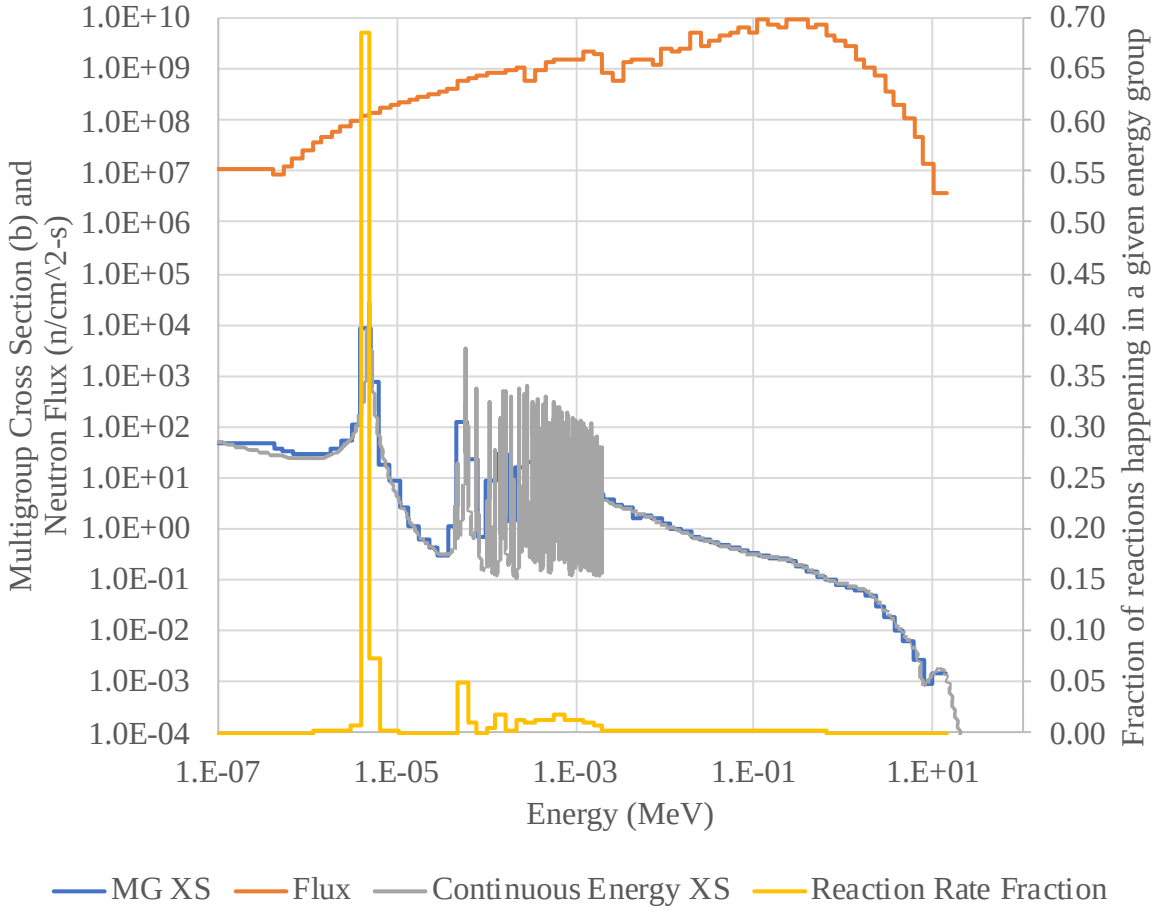

Figure C.2 70 group flux, cross section, and reaction rate for Au-197 neutron capture

Nuclear Science and Engineering Division
Argonne National Laboratory
9700 South Cass Avenue, Bldg. 208
Argonne, IL 60439

www.anl.gov

Argonne National Laboratory is a U.S. Department of Energy
laboratory managed by UChicago Argonne, LLC